npj | 2D materials and applications

Article

Published in partnership with FCT NOVA with the support of E-MRS

https://doi.org/10.1038/s41699-026-00721-1

Robust 2D-$SnSe_2$/TiO_2 S-scheme heterostructure for efficient neutral-pH oxygen evolution: experiments and DFT insights

Check for updates

Vittorio Ricci[1,2] ✉, Valentina Paolucci[1,2] ✉, Luigi Stagi[3], Luca Lozzi[4], Claudio Melis[5], Riccardo Dettori[5], Carlo Maria Carbonaro[5], Plinio Innocenzi[3], Luca Malfatti[3] & Carlo Cantalini[1,2]

Designing chemically robust photoanodes capable of efficient oxygen evolution reaction (OER) in neutral media remains a central challenge for practical photoelectrochemical (PEC) water splitting. By experiment and theory herein we report the PEC OER functionality of a durable and mechanistically well-defined 2D-$SnSe_2$/mesoporous TiO_2 heterostructure photoanode operating at pH 7. Highly crystalline 2D-$SnSe_2$ nanosheets (1.8 ± 0.1 μm lateral size and 100 ± 5 nm thickness) were solvothermally grown over mesoporous TiO_2 films, forming a layered 2D-$SnSe_2$/TiO_2 heterojunction, with efficient carrier transport and strong interfacial adhesion, solving the common delamination problem of 2D/TiO_2 systems. Under solar illumination, the 2D-$SnSe_2$/TiO_2 photoanode delivers a 16-fold higher current density than its single counterparts (0.80 mA/cm^2 at 1.7 V vs RHE), together with excellent operational stability (< 3% decay over 3 × 16 h continuous irradiation). Combining Mott–Schottky, valence-band XPS, and optical bandgap measurements with density functional theory (DFT), we reconstruct a defect-driven S-scheme charge-transfer mechanism, where oxygen vacancies in (110) TiO_2 shift band edges to promote selective electron–hole recombination at the interface. Finally, differential free adsorption energies calculations of the four OER intermediates over oxygen defective (110) TiO_2, indicate the OH* → O* transition as the potential-determining step. These results establish 2D-$SnSe_2$/TiO_2 as a stable, visible-light-responsive S-scheme heterostructure for neutral-pH OER, broadening the OER applications of group-IV chalcogenides MX_2 (M = Sn, Ge; X = S, Se)/TiO_2 photoanodes in neutral electrolytes.

Solar-to-hydrogen energy conversion by photo-electro-chemical (PEC) water splitting offers a straightforward, low-cost and promising route to produce sustainable hydrogen at the cathode, known as hydrogen evolution reaction (HER) and oxygen at the anode, known as oxygen evolution reaction (OER)[1,2]. Within this context, extensive efforts have been dedicated to researching new photoanode materials to accelerate the OER sluggish kinetics, while maintaining long-term stability under operation[3]. Although high HER/OER efficiencies are achieved in strong acid or alkaline media (pH 0/14), such environments severely compromise the chemical durability of most photoelectrodes, leading to rapid deactivation and structural degradation[4]. In this context, operating in neutral electrolytes is increasingly regarded as a desirable strategy to enhance device durability and compatibility with integrated PEC architectures. Nevertheless, achieving efficient OER activity at pH 7 remains scarcely investigated with respect to pH 14.

In the last decade, the synthesis of cost-effective and highly-performing OER photoanodes materials to substitute typical noble metal (Pt, Ir, Ru) OER catalysts has focused the attention to non-precious earth-abundant transition metal oxides[5], hydroxides and (oxy)hydroxides interfaces[6,7].

[1]Department of Industrial and Information Engineering and Economics, University of L'Aquila, P. Pontieri, 1 Monteluco di Roio, L'Aquila, Italy. [2]UdR INSTM of L'Aquila, L'Aquila, Italy. [3]Department of Engineering, University of Sassari, Via Vienna 2, Sassari, Italy. [4]Department of Physical and Chemical Sciences, University of L'Aquila, Via Vetoio, L'Aquila, Italy. [5]Department of Physics, University of Cagliari, Cittadella Universitaria di Monserrato, Monserrato, CA, Italy.
✉e-mail: vittorio.ricci@graduate.univaq.it; valentina.paolucci2@univaq.it

However, achieving efficient OER performances using individual metal oxides/hydroxides remains a substantial challenge due to their limited visible light (Vis) absorption, fast recombination of photoexcited carriers, low charge carrier mobility, and poor chemical stability. On this account, an effective strategy to enhance the HER/OER kinetic is represented by the synthesis of 2D/MO_x heterostructures (i.e. 2D layered materials/Metal Oxides), yielding superior performance with respect to the individual counterparts[8].

Among earth abundant semiconductors metal oxide (MO_x), especially TiO_2, is attractive for PEC applications due to is exceptional chemical stability[9] and resistance to photo-corrosion[10], representing the best interface to fabricate robust photoanodes/photocathodes. However, pure TiO_2 suffers from two critical limitations; a wide bandgap (≥ 3.2 eV), restricting absorption primarily to the UV fraction of sunlight (~ 4%), and (ii) fast recombination of photogenerated charge carriers on picosecond-to-nanosecond timescales[11], which dramatically reduces quantum efficiency. Coupling TiO_2 with visible-light responsive two-dimensional (2D) semiconductor co-catalyst with suitable band gaps (∼1.5 eV) and band alignment straddling the HER/OER potential (0/1.23 V vs RHE), represents an effective solution to increase the TiO_2 charge-separation in 2D/TiO_2 heterostructures.

Within the family of 2D layered transition metal dichalcogenides MX_2 (M = transition metal; X = S, Se, Te) and group-IV chalcogenides MX_2 (M = Sn, Ge; X = S, Se, Te), tin diselenide ($SnSe_2$) stands out as an ideal co-catalyst for 2D/TiO_2 heterostructures in solar energy applications, owing to its indirect band gap of ~1 eV[12] and high room-temperature electron mobility[13]. Beyond that, $SnSe_2$ shows promise as a catalytic interface across a broad range of application domains, including gas sensing[14], self-cleaning coatings[15], and hydrogen evolution reaction (HER) co-catalyst[16]. While group-IV SnS_2/TiO_2 heterostructures have been thoroughly investigated as potential photocatalysts (PCs)[17,18] and photo(electro)catalysts (PECs)[19,20], their selenide-based counterparts, such as $SnSe_2$/TiO_2 remain comparatively unexplored.

In this study, we synthesized highly crystalline 2D $SnSe_2$ nanoplatelets directly grown onto ordered mesoporous anatase TiO_2 thin films, forming a well-defined, layered $SnSe_2$/TiO_2 heterostructure with excellent surface adhesion and optimized electrical contact. The ~8 nm mesoporous TiO_2 framework[21,22] provides high surface area and nucleation sites for uniform $SnSe_2$ nanoplatelets growth. Through a combination of UV–Vis spectroscopy, linear sweep voltammetry, chopped-light chronoamperometry, XPS, Mott–Schottky analysis, and bandgap measurements, we demonstrate that this heterostructure delivers markedly enhanced OER activity under solar illumination at pH 7, achieving a 16-fold increase in photocurrent compared to bare TiO_2 and exhibiting remarkable long-term stability over extended irradiation cycles. To elucidate the underlying charge-transfer mechanism, we combine experimental measurements with density functional theory (DFT) calculations. Our results reveal the formation of an S-scheme band alignment driven by oxygen-defective TiO_2 (110) surfaces within the heterojunction. This configuration promotes efficient spatial separation of electrons and holes and aligns the band edges to simultaneously drive water oxidation and reduction half-reactions. Furthermore, DFT free-energy calculations identify the OH* → O* transformation as the OER potential-determining step on defective (110) TiO_2. Overall, this study establishes $SnSe_2$/TiO_2 heterostructures as a robust class of neutral-pH OER photoanodes and offers a practical route to exploit them with excellent stability in neutral pH.

Results

$SnSe_2$/TiO_2 heterostructure synthesis and characterization

We prepared $SnSe_2$/TiO_2 heterostructures by solvothermal growth of $SnSe_2$ nanoplatelets over sol-gel TiO_2 thin films, previously deposited by dip coating over Fluorine Doped Tin Oxide (FTO) electrodes and annealed in air at 400 °C[21]. The microstructural features of the FTO electrode are shown in Supplementary Information Fig. S1. Sol-gel TiO_2 thin films exhibit an average thickness of 224 ± 3 nm, measured by SEM cross section analysis displayed in Supplementary Information Fig. S2, and a homogenous, well organized, mesoporous structure (Fig. 1a), with pore-size distribution around 8 ± 1 nm (inset of Fig. 1a). The hydrothermal growth of $SnSe_2$ nanoplatelets over TiO_2 film was carried out according to two different routes (see section "Methods": "Solvothermal Growth of 2D-$SnSe_2$ platelets over mesoporous TiO_2 thin films").

Route 1. Starting from the SeO_2 precursor[23], a flower-like structure (Fig. 1b) is formed, consisting of a cluster of interconnected $SnSe_2$ nanosheets, with an average thickness of 72 ± 6 nm, 7 ± 1 μm lateral size, and aspect ratio (AR = average lateral size/average thickness of the nanoplatelets) of approximately 100 (see Supplementary Information Fig. S3 for statistics). These hierarchical heterostructure interfaces, beside the advantages to maximize the electrochemically active surface area, however, exhibit some limitations regarding the poor sticking of the agglomerated flakes over the substrate, hampering the durability of the photoelectrode in harsh electrolytes (pH = 0/14).

Route 2. Starting from Se precursor[24], flat 2D-$SnSe_2$ nanosheets are grown over the TiO_2 film (Fig. 1c). yielding a layered 2D-$SnSe_2$/TiO_2 heterostructure (inset of Fig. 1c). This enhanced architecture is a consequence of the higher synthesis temperature of Route 2 (220 °C) compared to Route 1 (180 °C). At 220 °C, metallic Se precursor melts forming a Se-oleic acid complex which dissolves in the reaction medium and eventually reacts with Sn^{4+} ions[24,25]. During this stage, it is likely that mesopores inside the TiO_2 film (~ 8 nm) act as nucleating sites for the 2D-$SnSe_2$ growth, while oleic acid works as a surfactant agent[22], improving the wettability of the TiO_2 surface. We finally prepared a homogeneous distribution of 2D-$SnSe_2$ nanoplatelets, covering 8.1 ± 0.5% of the underlying TiO_2 surface. Statistics from a set of 10 pictures, shown in Fig. 1d, exhibit an average size of the $SnSe_2$ particles of 1.8 ± 0.1 μm. AFM measurements (Fig. 1e) and related thicknesses distribution of the $SnSe_2$ nanoplates, shown in Fig. 1f, indicate an average thickness of 100 ± 5 nm, yielding an aspect ratio AR ~ 18. Grazing incidence (GI-XRD) X-ray diffraction patterns (Fig. 1g) of both TiO_2 (black line) and 2D-$SnSe_2$/TiO_2 (green line), exhibit a peak at $2\Theta = 25.3°$, corresponding to the (110) crystalline plane of the TiO_2 anatase phase (JCPDS Nr: 01-071-1167). Peaks located at $2\theta = 14.4°$, match with the (001) plane of crystalline $SnSe_2$ (JCPDS Nr: 96-154-8806), while peaks marked with (*) belong to the rutile phase of SnO_2 in the FTO substrate (JCPDS Nr: 01-077-0449).

The surface chemical composition of the 2D-$SnSe_2$ and TiO_2 films prepared on Si (100) substrates were investigated using X-ray Photoelectron Spectroscopy (XPS). Figure 1h,i display the detailed Sn-3d and Se-3d core-level spectra of 2D-$SnSe_2$, respectively. Specifically, the deconvolution of the Sn-3d core level spectrum of Fig. 1h reveals two distinct peaks. A major one located at 486.7 eV (green line) attributed to Sn^{4+} of $SnSe_2$[26,27] and a minor one located at 485.9 eV (magenta line), attributed to Sn^{2+} of SnSe[26]. The Se-3d core level spectrum in Fig. 1i, exhibits the characteristic features of Se $3d_{5/2}$ and Se $3d_{3/2}$ at 53.5 eV and 54.6 eV, corresponding, as previously reported[27], to Se^{2+}. No traces of Se^0 or SeO_2 are detected in the Se 3d region, specifically at 56.0 eV (Se^0)[28] and 59.2 eV (SeO_2)[29]. The O-1s core level spectrum of $SnSe_2$ (shown in Supplementary Information Fig. S4) exhibits a single peak at 532.7 eV, which can be assigned to either adsorbed water or surface hydroxyl groups[30,31]. Moreover, the O-1s core level spectrum features of $SnSe_2$ rule out the formation of oxidized species like SnO_2 and SeO_2 with energies located at 531.4 eV[28] and 532.0 eV[28,29], corresponding to the formation of Sn-O and Se-O bonds.

Figure 1l,m displays the detailed Ti-2p and O-1s core-level spectra of TiO_2. The Ti $2p_{3/2}$ and Ti $2p_{1/2}$ components located at 458.7 and 464.6 eV (Fig. 1l) well match the Ti–O binding energies of TiO_2[32]. Additionally, the deconvolution of the Ti 2p spectrum reveals a minor Ti^{3+} contribution, which can be associated to a defective state and allows for a quantitative estimation of the of oxygen vacancies concentration, as recently reported[33].

Specifically, using the integrated areas of Ti^{4+} and Ti^{3+}corrected for atomic sensitivity factors, the relative Ti^{3+} fraction is calculated as $f_{Ti3+} = A_{Ti3+} / (A_{Ti3+} + A_{Ti4+})$, resulting in a value of 0.024, corresponding to a defect concentration measured by area ratio of Ti^{3+} peak of 2.4%. Assuming

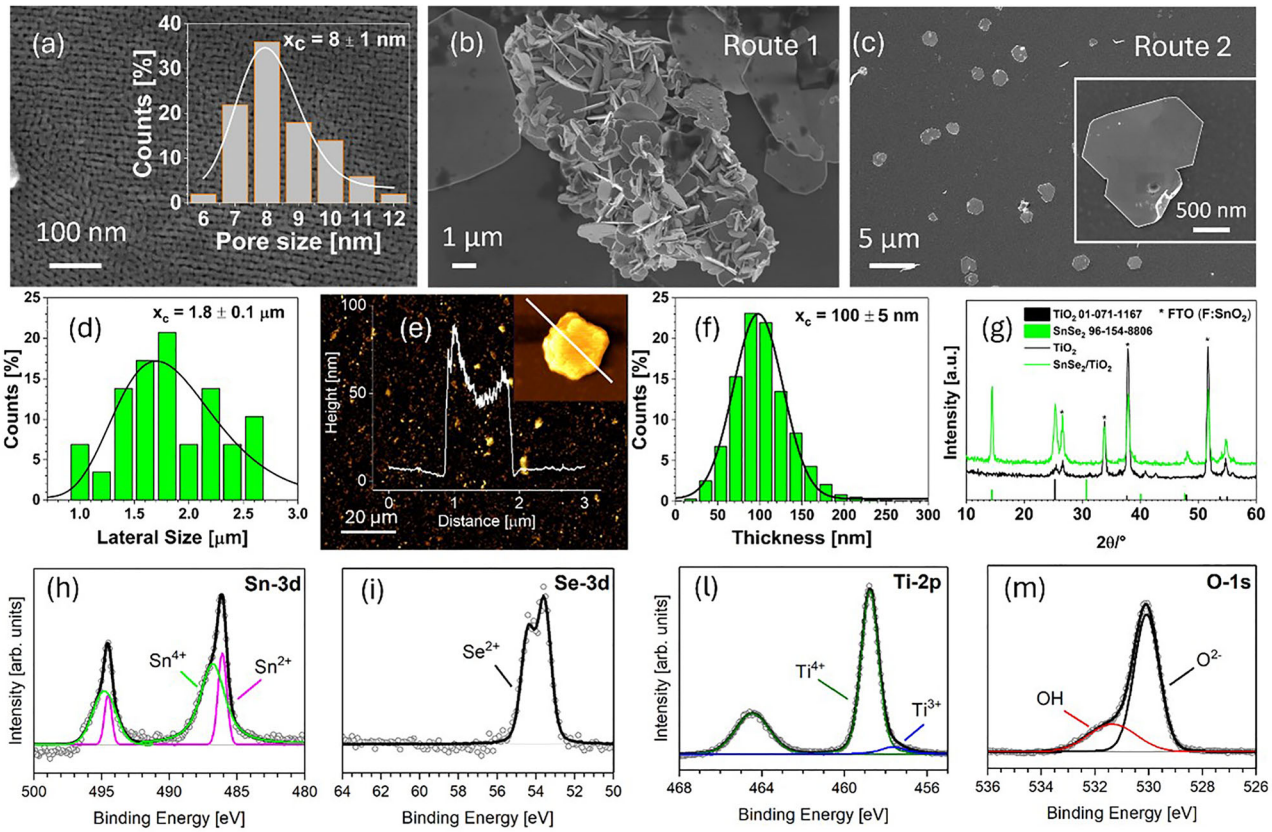


Fig. 1 | Microstructural Characterization of the 2D-$SnSe_2$/TiO_2 heterostructure. SEM images of **a** TiO_2 film; inset: statistical pore size distribution; **b** flower-like 2D-$SnSe_2$ agglomerated nanosheets synthesized by Route 1; **c** 2D-$SnSe_2$ nanosheets synthesized over TiO_2 (Route 2); inset: single 2D-$SnSe_2$ nanosheet over TiO_2; **d** SEM lateral size distribution of 2D-$SnSe_2$ nanosheets; **e** AFM image and thickness profile of a 2D-$SnSe_2$ nanosheet; **f** AFM thickness distribution of 2D-$SnSe_2$ nanosheets; **g** Grazing Incidence GI-XRD spectra of TiO_2 and 2D-$SnSe_2$/TiO_2. Peaks corresponding to FTO substrate are highlighted by "*"; XPS spectra of **h** Sn-3d and **i** Se-3d core level spectra of 2D-$SnSe_2$, **l** Ti-2p and **m** O-1s of TiO_2 (fitted experimental data are indicated by black lines).

local charge neutrality, where each oxygen vacancy is charge-compensated by the reduction of two Ti^{4+} sites[33], the non-stoichiometry parameter δ ($\approx f_{Ti3+}/2$) in $TiO_{2-\delta}$ is estimated as 0.012. Also, the deconvolution of the O-1s spectrum (Fig. 1m) reveals two distinct components located at 530.1 eV and 531.4 eV, respectively, attributed to the lattice oxygen of TiO_2 (black line)[32] and hydroxyl groups bonded to Ti^{4+} cations in oxygen deficient regions, in agreement with earlier studies[34].

Finally, information deriving from SEM-EDX elemental maps of the $SnSe_2$/TiO_2 heterostructure, reported in Supplementary Information Fig. S5, exhibits O and Ti signals fully attributed to the TiO_2 film, and Sn and Se belonging to $SnSe_2$, confirming the absence of oxygen over the $SnSe_2$ flake. In conclusion, by adopting synthesis Route 2, we successfully synthesized a 2D-$SnSe_2$ /TiO_2 heterostructure exhibiting precise microstructural features, well-defined chemical composition, and clearly identified crystalline structures. Moreover, the layered architecture of the 2D-$SnSe_2$ /TiO_2 heterostructure enhances the adhesion of $SnSe_2$ nanoplatelets over TiO_2 surface, thereby facilitating more efficient charge transfer across the heterojunction and long-lasting durability of the photoanode.

Optical characterization

The optical characteristics of bare FTO, TiO_2, $SnSe_2$ and $SnSe_2$/TiO_2 samples have been characterized by UV-Vis absorbance and Diffuse Reflectance Spectroscopy (DRS), and the results shown in Fig. 2. The TiO_2 sample shows slightly increased absorption in the whole UV-Vis spectrum if compared to bare FTO (respectively black and blue lines of Fig. 2a), with a well-defined onset at 340 nm, in accordance with previous research[35]. The $SnSe_2$ spectrum (red line) exhibits an approximately uniform light absorption in the whole UV-Vis range, in accordance with previously reported DC sputter-fabricated $SnSe_2$ thin films[36]. Unsurprisingly, the slight peaks of the $SnSe_2$ spectrum at around 500 and 420 nm can be ascribed to the FTO substrate behaviour, as confirmed by the FTO UV-Vis spectrum (blue line). Finally, the absorption spectrum of 2D-$SnSe_2$/TiO_2 heterostructure (green line of Fig. 2a) shares similar features to TiO_2, with the incorporation of $SnSe_2$ nanoplatelets proving beneficial by increasing light absorption in the 400–800 nm range[36].

The optical bandgaps of TiO_2 and 2D-$SnSe_2$ (Fig. 2b), utilizing diffuse reflectance spectroscopy (DRS) data (reported in Supplementary Information Fig. S6), have been estimated by applying the Tauc plot method[37]. Specifically, DRS spectra have been converted to the Kubelka-Munk function $F(R)$ and then used to compute the corresponding Tauc plots (Eq. 1):

$$(F(R)h\nu)^{1/\gamma} = B(h\nu - E_g) \quad (1)$$

With h representing the Planck's constant, ν the incident photons' energies, B a constant and E_g the semiconductor's optical bandgap energy. The E_g values of TiO_2 and 2D-$SnSe_2$, shown in Fig. 2b, yield 3.3 and 1.7 eV respectively, congruently with sol-gel deposited TiO_2[38] and sputter-fabricated $SnSe_2$[36] films. In conclusion, UV-Vis and DRS confirm the improved UV-Vis absorbance of 2D-TiO_2/$SnSe_2$ heterostructure compared to TiO_2 alone, supporting the improved solar harvesting capability of the heterojunction if compared to the single materials.

Photo-electro-catalytic (PEC) characterization

Oxygen Evolution Reaction (OER) PEC response of $SnSe_2$, TiO_2 and $SnSe_2$/TiO_2 were characterized by Linear Sweep Voltammetry (LSV) both in dark and different light sources (at UV = 365 nm, PB = 470 nm, Green = 530 nm,

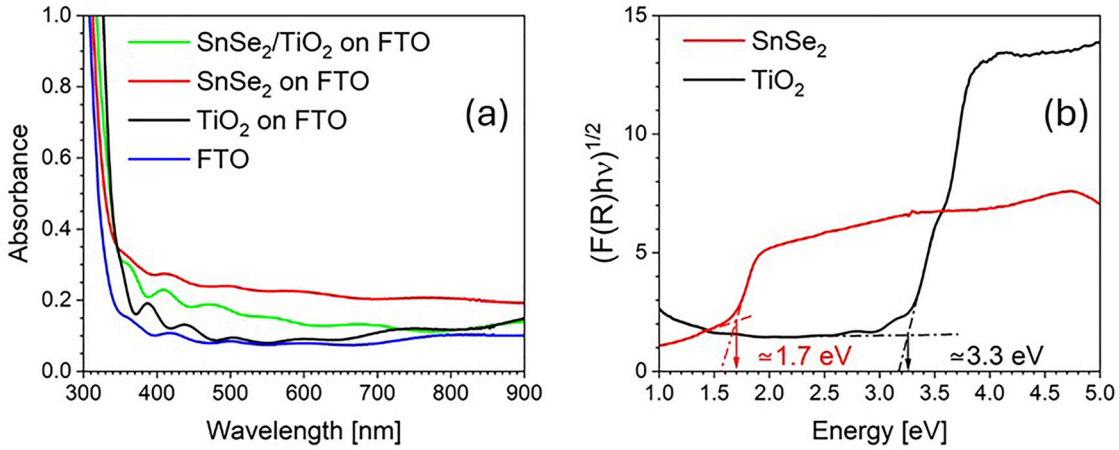


Fig. 2 | Optical Characterization of the 2D-$SnSe_2$/TiO_2 heterostructure. UV-Vis absorbance spectra of **a** bare FTO substrate (blue line), TiO_2 (black line), 2D-$SnSe_2$ (red line), and 2D-$SnSe_2$/TiO_2 (green line) deposited over FTO in the 300–900 nm range. **b** Tauc plots of TiO_2 (black line) and 2D-$SnSe_2$ (red line) on quartz substrates, calculated from DRS data.

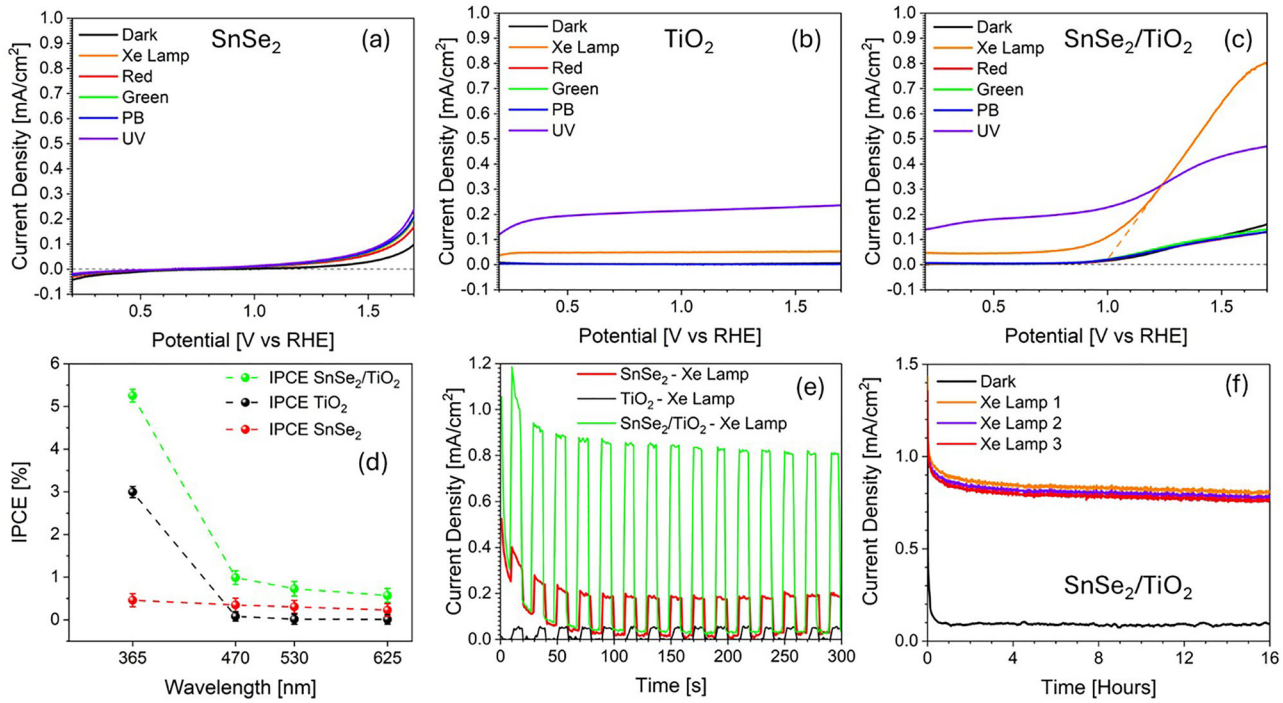


Fig. 3 | PEC OER Characterization of the 2D-$SnSe_2$/TiO_2 heterostructure. LSV curves at a scan speed of 200 mV/s and different illumination conditions of **a** 2D-$SnSe_2$, **b** TiO_2 and **c** 2D-$SnSe_2$/TiO_2; **d** IPCE curves of 2D-$SnSe_2$ (red line), TiO_2 (black line), 2D-$SnSe_2$/TiO_2 heterostructure (green line). The values and corresponding standard deviations were calculated from three independent LSV measurements for each photoanode. **e** Chronoamperometric (CA) measurements under chopped illumination (chopping light every 10 seconds) of 2D-$SnSe_2$ (red line), TiO_2 (black line) and 2D-$SnSe_2$/TiO_2 (green line), recorded at a constant potential of 1.7 V vs RHE; **f** Chronoamperometric (CA) long-term reproducibility measurements of 2D-$SnSe_2$/TiO_2 under constant irradiation conditions. Dark (black line), Solar light (orange, magenta and red lines), corresponding to three repeated tests each lasting 16 h (first: orange, second: magenta, third: red), recorded at a constant potential of 1.7 V vs RHE.

Red = 625 nm), set at the same irradiance of 250 μW/mm^2, and utilizing a solar light simulator corresponding to 1 sun intensity (1000 μW/mm^2), as described in section "Methods": "Photoelectrochemical Characterization". Specifically, the oxygen evolution reaction $4OH^- \rightarrow O_{2(g)} + 2H_2O_{(l)} + 4e^-$ at pH 7 (starting at a theoretical potential of 1.23 V vs RHE = 0.817 V vs SHE), was investigated recording the current density [mA/cm^2] vs potential [V vs RHE] in the 0.2 to 1.7 V vs RHE range. To confirm that the observed PEC-OER activity do not originate from the FTO substrate, LSV curves of bare FTO were included in Supplementary Information Fig. S7, showing negligible activity under both dark and illuminated conditions. As shown in Fig. 3a, 2D-$SnSe_2$ film exhibits negligible OER activity under dark conditions, whereas a modest increase in current density emerges under UV-Vis irradiation departing from 1.1 V. Specifically, at an applied potential of 1.7 V, the current density rises from 0.10 mA/cm^2, following the sequence: Dark < Red < Solar < Green < PB < UV, reaching a maximum of 0.23 mA/cm^2 under UV light illumination. Considering that 2D-$SnSe_2$ measured bandgap of Fig. 2b is 1.7 eV, corresponding to λ ~ 730 nm, all the investigated light sources are potentially capable to trigger electron-hole

Table 1 | Comparison of the PEC OER performances of TiO_2 heterostructures

Heterostructure	Current density [mA/cm^2] (1 sun irradiance) and @ 1.5 V vs RHE	pH	Electrolyte	Ref.
SnS_2 nanosheets (NSs)/TiO_2 nanotubes	1.40	7	0.5 M Na_2SO_4	20
SnS_2 nanosheets (NSs)/TiO_2 nanotubes	4.00	7	0.5 M Na_2SO_4	41
BiOI NSs/mesoporous TiO_2	0.08	7	$H_2PO_4^-/HPO_4^{2-}$	75
ALD-MoS_2/TiO_2 nanotubes	0.03	7	0.5 M Na_2SO_4	39
$PtSe_2$ naonflakes /TiO_2 nanotubes	0.70	7	0.5 M Na_2SO_4	40
CoPi /mesoporous TiO_2	0.05	7	0.1 M $H_2PO_4^-/HPO_4^{2-}$	76
g-C_3N_4/TiO_2 nanotubes	1.00	7	0.1 M Na_2SO_4	77
Carbon Dots (CDs)/ mesoporous TiO_2	1.00	7	0.1 M $H_2PO_4^-/HPO_4^{2-}$	35
2D-$SnSe_2$/ mesoporous TiO_2	0.65	7	0.5 M Na_2SO_4	This work

Data are compared setting the current density at 1.5 [mA/cm^2] vs RHE potential and 1 sun (1000 W/m^2) illumination. The pH and electrolyte used in each work are also reported.

pairs generation, eventually explaining the increase of the current density of Fig. 3a.

TiO_2 film photoanode under dark and Vis irradiation shows no PEC OER response, as attested by the evolution of flat lines coincident with 0.00 mA/cm^2 in Fig. 3b. Unsurprisingly, UV light triggers PEC OER response in a broad potential range (i.e. 0.3–1.7 V), yielding a current density of 0.23 mA/cm^2 at 1.7 V, comparable to $SnSe_2$. This behaviour is congruent with electron-hole pairs generation in the TiO_2 band gap (the optical bandgap of TiO_2 ($\geq$ 3.2 eV)[38] is ~ 3.3 eV, see Fig. 2b), triggered by UV light stimulation at λ = 365 nm. Additionally, the TiO_2 PEC OER response to solar light irradiation (orange line) yields a current of 0.05 mA/cm^2 at 1.7 V, which is smaller than that recorded under UV light (violet line), on account of the limited fraction (~ 4%) of the UV light component in the solar spectrum.

Remarkably, under solar light illumination (orange line in Fig. 3c), the 2D-$SnSe_2$/TiO_2 heterostructure achieves a current density of 0.80 mA/cm^2 at 1.7 V, which is ~16 times higher than those of the 2D-$SnSe_2$ and TiO_2 individual counterparts, with an associated onset potential of ~1.0 V vs RHE (i.e. tangent of the orange line intercepting zero current density in Fig. 3c). Similarly, under UV light illumination, the 2D-$SnSe_2$/TiO_2 heterostructure exhibits a PEC OER current density of 0.48 mA/cm^2 at 1.7 V, representing an approximately two-fold enhancement compared to the individual 2D-$SnSe_2$ and TiO_2 photoelectrodes. In this perspective, the ~16-fold enhancement of the PEC OER response of the 2D-$SnSe_2$/TiO_2 heterostructure with respect to TiO_2 under solar light irradiation, compared to the ~2-fold increase observed under UV light, confirms the presence of a synergistic charge transfer mechanism between TiO_2 and 2D-$SnSe_2$ co-catalyst, which will be comprehensively discussed in the following paragraphs. Figure 3d shows the Incident Photon-to-Current Conversion Efficiency (IPCE) calculated at 1.23 V vs RHE for the TiO_2, 2D-$SnSe_2$, and 2D-$SnSe_2$/TiO_2 heterostructure photoanodes, deriving from the LSV curves of Fig. 3a–c. IPCE values were determined using the standard equation (Eq. 2):

$$IPCE\% = \frac{1240 * I}{P(\lambda) * \lambda} * 100 \quad (2)$$

where I is the photocurrent density [mA/cm^2], $P(\lambda)$ is the incident light power density [mW/cm^2], and λ is the excitation wavelength [nm]. Congruent with the LSV curves, 2D-$SnSe_2$ (red line) exhibits a limited yet constant IPCE% regardless of the excitation wavelength, while TiO_2 shows significant IPCE% only in the UV region (black line). Remarkably, the overall IPCE% of the 2D-$SnSe_2$/TiO_2 heterostructure (green line), is significantly shifted to higher values, attesting the occurrence of an effective photoresponse in the whole UV-Vis range. Moreover, the specific IPCE% of the 2D-$SnSe_2$/TiO_2 heterostructure reaches at 365 nm ~6% compared to ~3% of TiO_2. Considering that the coverage of the 2D-$SnSe_2$ is ~ 8% (Fig. 1c), this improvement indicates that even a limited extension of 2D-$SnSe_2$/TiO_2 heterojunctions is sufficient to enhance interfacial charge separation and UV-Vis light sensitization. To compare the PEC OER performance of the synthesized 2D-$SnSe_2$/TiO_2 heterostructure with analogous 2D/TiO_2 systems reported in the literature, relevant data were collected and normalized to ensure consistent experimental conditions. This comparison is, however, affected by numerous unknown variables, including electrochemically active surface area (ECSA), potential range, sweep rate, light irradiance, aeration state, agitation conditions, etc. Given these limitations, Table 1 shows a comparison of selected features of previously investigated heterostructure interfaces. Setting a common base at pH = 7, 0.5 M Na_2SO_4 or 0.1 M $H_2PO_4^-/HPO_4^{2-}$ electrolytes and 1.5 V vs RHE potential, it turns out that the PEC OER performance of our 2D-$SnSe_2$/TiO_2 heterostructure is better or in line with those corresponding to refs. 39,40, while being significantly smaller than flower-like SnS_2 hierarchical structures grown on TiO_2 nanotubes[20,41]. It is noted that flower-like 2D-SnS_2/TiO_2 heterojunction or 2D-$SnSe_2$/TiO_2 synthesized by Route 1 (Fig. 1b), offer the advantage of higher OER current density, primarily due to their increased surface area. However, these structures suffer from poor adhesion, which accelerates performance degradation in aqueous environments. Conversely, the layered nanoplatelet architecture obtained by Route 2 (Fig. 1c), intimately anchored within a mesoporous TiO_2 matrix, solve the common delamination problem of 2D/TiO_2 heterostructures, a feature of relevance for reliable long-term operation under practical conditions.

The short and long-term reproducibility of the OER performances of photoanodes interfaces represent a key issue for the exploitation of solar harvesting materials. Remarkably, operating at pH = 7 represents a considerable advantage as respect to strong acidic or alkaline environments, which may result in a longer lifetime of the solar electrolyser. To verify measurements consistency, the short-term reproducibility of the PEC OER responses of 2D-$SnSe_2$ (red line), TiO_2 (black line), and 2D-$SnSe_2$/TiO_2 heterojunction (green line) is shown in Fig. 3e. The data were obtained via chopped light chronoamperometry (CA) conducted over 300 seconds, with alternating dark/solar illumination cycles of 10 s, at a fixed potential of 1.7 V vs RHE. Irradiating with solar light, the $SnSe_2$ current density reaches 0.40 mA/cm^2 in the first pulse and then asymptotically decreases to 0.23 mA/cm^2 in the last. Differently, for TiO_2 a constant value of 0.05 mA/cm^2 is obtained in the whole test. Finally, 2D-$SnSe_2$/TiO_2 exhibit an initial value of 1.20 mA/cm^2 that asymptotically decreases to 0.80 mA/cm^2 at the end of the test, matching the same value of the current density recorded at 1.7 V in Fig. 3c. Finally, long term stability tests of the PEC OER capabilities the $SnSe_2$/TiO_2 heterostructure were performed under continuous solar illumination by running three repeated chronoamperometric tests lasting 16 h each (at 1.7 V potential), while recording the current density, as shown in Fig. 3f. The 2D-$SnSe_2$/TiO_2 heterostructure shows excellent current stability over time with an average photocurrent density of 0.80 mA/cm^2, with a negligible standard deviation of ± 0.02 mA/cm^2 ($\leq$ 3%), confirming the outstanding long term OER performance of the photoanode electrode in neutral solutions.

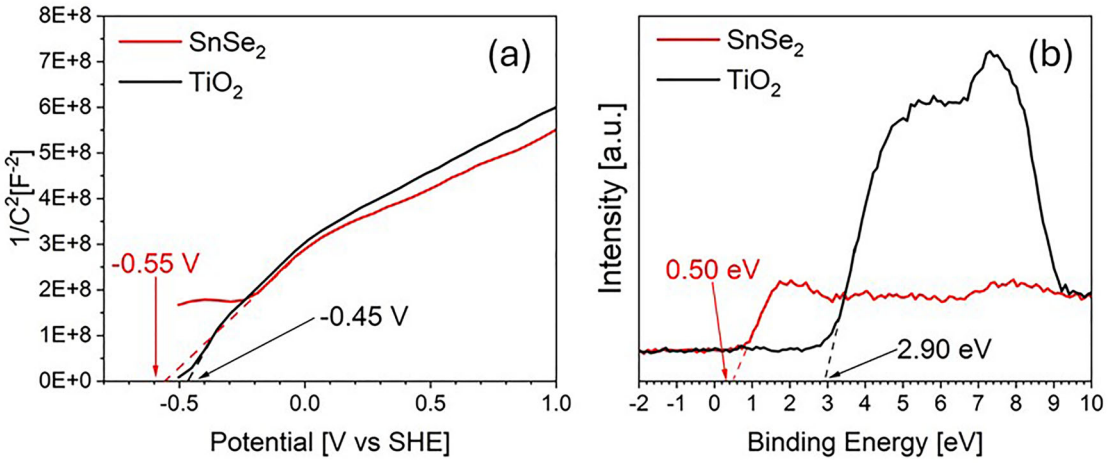


Fig. 4 | Mott Schottky Plots and VB-XPS of 2D-$SnSe_2$ and TiO_2. a Mott Schottky curves of 2D-$SnSe_2$ (red line) and TiO_2 (black line) deposited over FTO substrates in Na_2SO_4 0.5 M electrolyte. **b** Valence Band XPS spectra of $SnSe_2$ (red line) and TiO_2 (black line) deposited over Si substrates.

In addition to the excellent long-term stability of the photoelectrochemical (PEC) performance of the $SnSe_2/TiO_2$ heterostructure, as demonstrated by the chronoamperometric measurements shown in Fig. 3f, we have further substantiated the stability of the system by comparing the microstructural (SEM) and chemical (Raman spectroscopy) characteristics of the $SnSe_2/TiO_2$ heterostructure before and after the long-term chronoamperometry test, as shown in Supporting Information Figs. S8,9. SEM analysis (Fig. S8) shows no significant changes in the morphology or distribution of the $SnSe_2$ flakes after 3×16 h repeated continuous PEC operation, indicating the absence of surface degradation. Moreover, EDX mapping reveals a consistent elemental distribution, with no detectable oxygen signal associated with environmental degradation of the $SnSe_2$ domains, thus excluding the formation of oxidized Sn-based phases. Raman spectra of the heterostructures collected before and after test, shown in Supporting Information Fig. S9, were acquired by confocal microscopy using a 100x objective. The focal plane was fixed on the top surface of the heterostructures to investigate possible chemical changes in the $SnSe_2$ flakes deposited on the mesoporous titania film. The spectra display two characteristic bands at 118 and 185 cm^{-1}, assigned to the A_{1g} and E_g vibrational modes of $SnSe_2$. Importantly, no evidence of $SnSe_2$ oxidation, which would be detectable in the region around 700 cm^{-1}, is observed. The two spectra are nearly identical, except for the appearance, after chronoamperometry, of a weak Raman band at ~145 cm^{-1}, attributable to anatase TiO_2. This feature is most likely due to slight differences in the focal conditions between the two measurements, which allowed partial probing of the shallow oxide layer underneath the $SnSe_2$ flakes. Overall, the combined SEM, EDX, and Raman results consistently indicate that the $SnSe_2/TiO_2$ heterostructure retains both its microstructural integrity and chemical composition after extended PEC operation, in line with the highly stable photocurrent behaviour observed in the long-term chronoamperometric tests.

Band structure model of the $SnSe_2/TiO_2$ heterostructure

To demonstrate the enhanced PEC OER activity of the $SnSe_2/TiO_2$ heterostructure as respect to single 2D-$SnSe_2$ and TiO_2 interfaces, we built a model of the heterojunction based on experimental measurements. The model requires as input data the Fermi Levels (FL), Valence Band Maximum (E_{VBM}), and Conduction Band Minimum (E_{CBM}) energy positions of both the 2D-$SnSe_2$ and TiO_2 single interfaces. These experimental values were obtained by Mott Schottky (MS)[42], Valence Band XPS (VB-XPS) and bandgap (BG) measurements. Specifically, Mott Schottky (MS) plots, shown in Fig. 4a, confirm the *n*-type semiconducting nature of both materials by the positive slopes of the dotted lines, as previously reported[35,43]. By extrapolating the intercept of the MS plots, Fermi levels of −0.45 V and −0.55 V vs SHE were obtained, corresponding to the flat band potentials of the TiO_2 and 2D-$SnSe_2$ photoanodes immersed in Na_2SO_4 0.5 M. These data well agree with previous investigations of anatase TiO_2[44] and CVD grown $SnSe_2$[20] films in the same electrolyte conditions.

By linear extrapolation of the onset of the XPS spectra[32] of Fig. 4b, the valence band positions ($E_{VB\text{-}XPS}$) with respect to the Fermi Level were obtained, providing 2.90 and 0.50 eV for TiO_2 and 2D-$SnSe_2$, respectively. These findings well match the values of 3.0 eV for an anatase-rutile mixed TiO_2 phase[45] and 0.5 eV for CVD-grown $SnSe_2$[46]. The valence band maximum energy position (E_{VBM}) in the SHE scale was then calculated using Eq. 3:

$$E_{VBM} = FL + E_{VB-XPS}[\text{V vs SHE}] \quad (3)$$

yielding the values of 2.45 and -0.05 V vs SHE for TiO_2 and 2D-$SnSe_2$. Finally, the conduction band minimum energy position (E_{CBM}) has been calculated using Eq. 4:

$$E_{CBM} = E_{VBM} - E_g[\text{V vs SHE}] \quad (4)$$

Substituting in Eq. 4 the optical bandgap energies E_g [eV], estimated in Fig. 2b, the calculated E_{CBM} values are –0.85 and −1.75 V vs SHE for TiO_2 and 2D-$SnSe_2$, respectively. Based on these experimental findings, the band edge positions diagrams for TiO_2 and $SnSe_2$ before (left-hand side) and after establishing electric contact (right-hand side), are presented in Fig. 5a and Fig. 5b respectively, together with the equilibrium potential for the Oxygen Evolution Reaction (OER) at pH 7 (red dashed line of Fig. 5b). According to Fig. 5a (before electric contact), both the E_{VBM} and the E_{CBM} of TiO_2 are more positive than the corresponding values of $SnSe_2$. After electric contact (Fig. 5b), Fermi levels align (black dashed line). Electrons (the majority charge carriers for both *n*-type materials) move from 2D-$SnSe_2$ to TiO_2 to achieve equalization of their Fermi Levels, causing an upward band bending in $SnSe_2$ and a downward band bending in TiO_2[47], as indicated in Fig. 5b. In conclusion, an electric field *E* is established at the heterostructure interface, directed from 2D-$SnSe_2$ towards TiO_2.

PEC-OER charge transfer mechanism under UV-VIS light irradiation

In Fig. 6 the charge transfer mechanism of the PEC-OER of the 2D-$SnSe_2$/TiO_2 heterojunction is drawn. Upon UV-Vis light illumination, absorbed TiO_2 and 2D-$SnSe_2$ photons, with $h\nu \geq E_g$, excite electrons to the respective conduction bands (CB) leaving holes in the valence bands (VB). According to the band edge positions of Fig. 5b (right-hand side), the VB potential of TiO_2 is more positive than $E = 0.817$ V vs SHE, corresponding to the oxidation of OH^- to produce O_2 (red dashed line of Fig. 6). It turns out that TiO_2

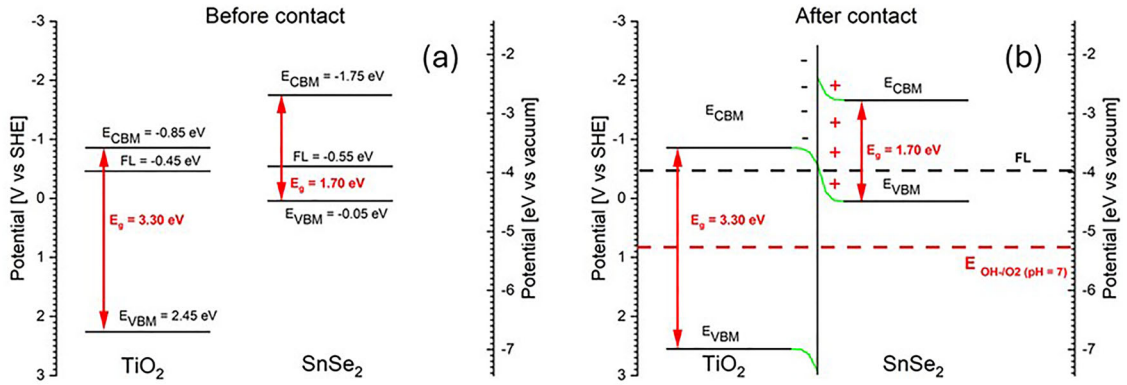


Fig. 5 | Band Structure of the 2D-$SnSe_2$/TiO_2 heterojunction. Band Structure of the 2D-$SnSe_2$/TiO_2 heterojunction before **a** and after **b** electric contact.

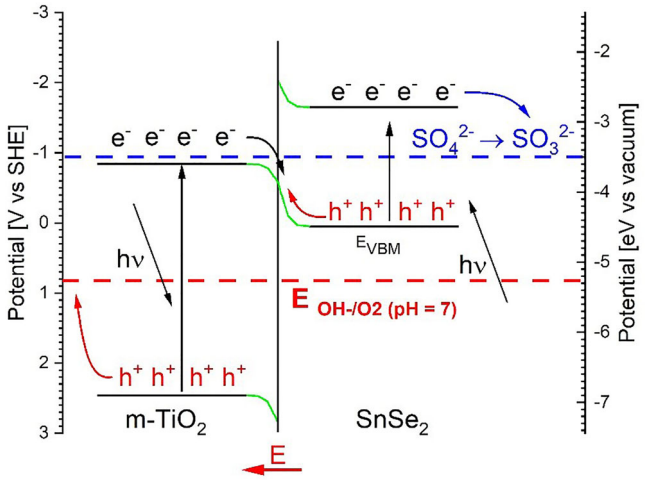


Fig. 6 | Schematization of the charge transfer mechanism of the 2D-$SnSe_2$/TiO_2 heterojunction for PEC-OER.

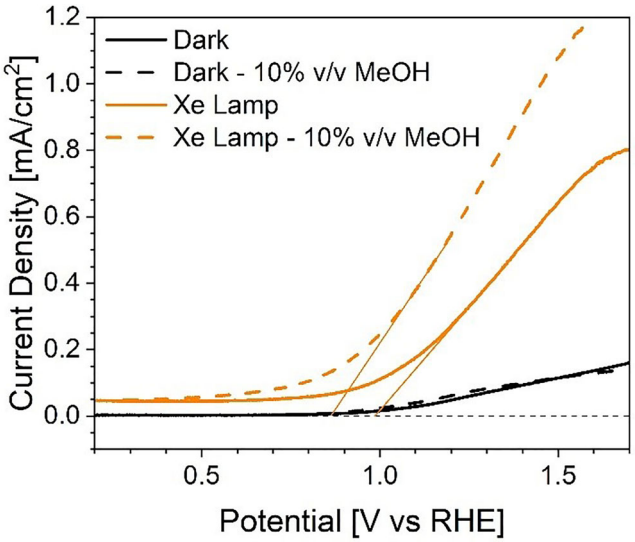


Fig. 7 | LSV curves of the 2D-$SnSe_2$/TiO_2 photoelectrode in dark (black lines) and solar illuminated conditions (orange lines), in absence (continuous lines) and presence (dashed lines) of methanol 10% vol/vol in the 0.5 M Na_2SO_4 test electrolyte.

VB holes ($h+$ in Fig. 6) have the right potential to be consumed (alongside the red arrow of Fig. 6) according to the reaction in Eq. 5:

$$4OH^- + 4h^+ \rightarrow O_{2(g)} + 2H_2O_{(l)} \quad (5)$$

At same time, the built-in electric field drives electrons/holes towards the heterojunction interface. Consequently, the 2D-$SnSe_2$ UV-Vis generated VB holes move backwards to the TiO_2 interface, recombining with TiO_2 CB electrons. According to the band structure positions of Fig. 5b (right-hand side), the CB potential of 2D-$SnSe_2$ is more negative than the E° = -0.93 V vs SHE potential, corresponding to the reduction of the electrolyte's SO_4^{2-} to SO_3^{2-} (blue dashed line in Fig. 6). It turns out that $SnSe_2$ CB electrons (e^- in Fig. 6) have the right potential to be consumed (blue arrow of Fig. 6) to reduce SO_4^{2-} to SO_3^{2-}, according to the reaction in Eq. 6

$$SO_4^{2-} + H_2O + 2e^- \rightarrow SO_3^{2-} + 2OH^- \quad (6)$$

To further substantiate the proposed model, we monitored the concentration of SO_4^{2-} anions in the electrolyte every 4 h by performing three independent long-term chronoamperometric measurements, as described in section "Methods": "Measure of [SO_4^{2-}] as a function of reaction time", each lasting 16 h, in the same fashion as those reported in Fig. 3f. As shown in Supplementary Information Fig. S10, the initial SO_4^{2-} concentration decreased after 16 h by ~ 2%, thereby supporting the scheme of Fig. 6. Moreover, as an additional proof of the participation of holes (h^+) to the OH^- oxidation reaction (Eq. 5), we performed LSV measurements in dark and illuminated conditions adding methanol (10% vol/vol) to the 0.5 M Na_2SO_4 test electrolyte, on account of its proved hole scavenging properties in the 4 to 40%vol/vol range for mesoporous anatase TiO_2 photoanodes[48].

As visible from Fig. 7, a definite increase in photocurrent density is observed in solar light illuminated conditions (compare dashed and continuous orange lines). Specifically, current density values at 1.5 V vs RHE potential increased from 0.65 mA/cm² to 1.07 mA/cm² in the absence/presence of methanol, respectively. Additionally, the onset of the photocurrent density decreased from approximately 1.00 V vs RHE to 0.85 V vs RHE (compare tangents to the continuous and dashed orange lines, respectively), in agreement with previous works[49,50]. These effects can be ascribed to the higher methanol oxidation reaction rate with respect to the oxygen evolution reaction rate[48], which results in improved photoinduced charge separation and charge transfer[49] from the 2D-$SnSe_2$/TiO_2 photoanode to the electrolyte species. This suggests that in the 2D-$SnSe_2$/TiO_2 photoanode holes (h^+) are the photoinduced charges participating to the oxygen evolution reaction (Eq. 5), while photoexcited electrons are consumed by the SO_4^{2-} reduction reaction (Eq. 6), further corroborating the S-Scheme mechanism proposed in Fig. 6.

In conclusion, the synergistic PEC OER response of Fig. 3c follows a S-scheme mechanism, found in photocatalytic (PC) and photoeletrocatalytic (PEC) applications[51]. Specifically, the 2D-$SnSe_2$/TiO_2 heterojunction is effective to boost PEC OER considering: (i) the capability of 2D-$SnSe_2$ and TiO_2 to absorb incident photons in the UV-Vis range and to generate electrons-holes pairs, (ii) the effectiveness of the 2D-$SnSe_2$

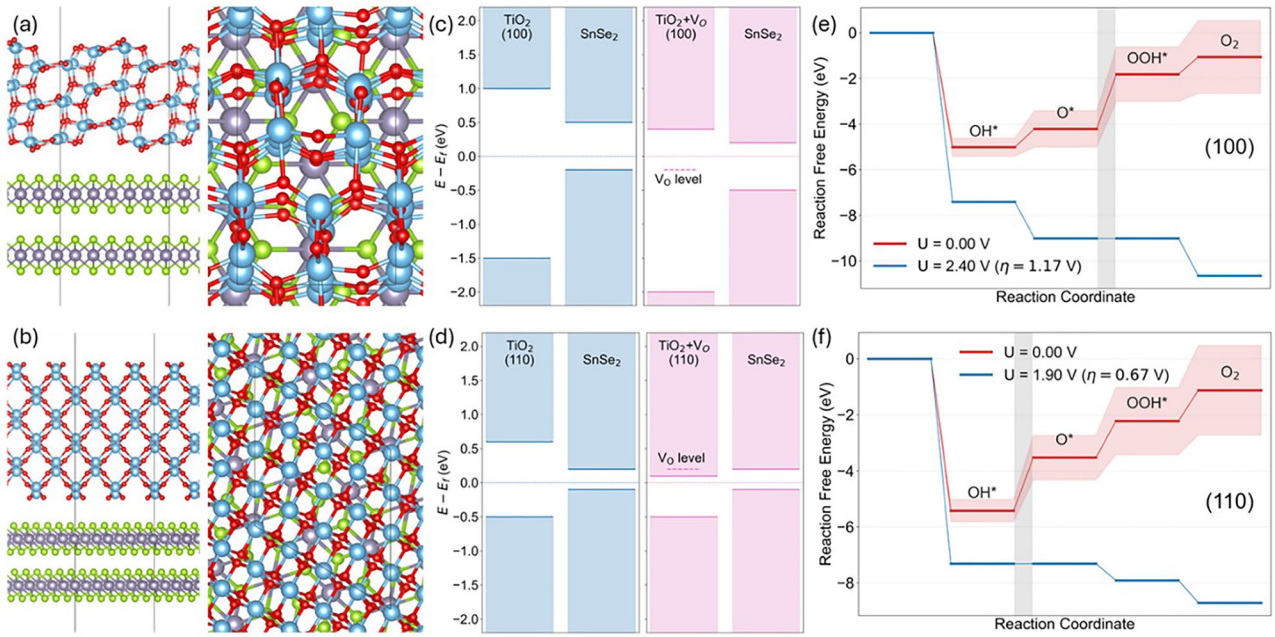


Fig. 8 | Computational model of the 2D-$SnSe_2$/TiO_2 heterostructure. a, **b** Side and top views of the (100) and (110) oriented TiO_2 + $SnSe_2$ structures; (red ● O; light blue ● Ti; mauve ● Sn; green ● Se) **c**, **d** Band alignment computed from the projected DOS of the (100) and (110) oriented heterostructures. Blue: non-defective TiO_2 based heterostructure. Pink: defective TiO_2 based heterostructure; **e**, **f** Reaction free energies (red lines) corresponding to the four OH*, O*, OOH*, O_2 intermediates over oxygen defective (100) and (110) TiO_2 using the CHE approach, without any simulated applied potential. The shaded grey region identifies the Potential Determining Step (PDS), while the shaded red area represents the associated uncertainty. Reaction free energies (blue lines) corresponding to the four OH*, O*, OOH*, O_2 intermediates over oxygen defective (100) and (110) TiO_2 using the CHE approach and a simulated applied potential.

co-catalyst to reduce charge carriers recombination in TiO_2, (iii) the 2D-$SnSe_2$/TiO_2 heterostructure VB/CB positioning, straddling the potential for OH^- to O_2 oxidation and that for the reduction of SO_4^{2-} to SO_3^{2-}.

Computational model of the OER energy pathways over $SnSe_2$/TiO_2 heterostructure

Starting from the bulk structures of $SnSe_2$ and TiO_2, density functional theory (DFT) calculations (as detailed in "Methods": "Computation Model"), were conducted featuring: defect-free and oxygen (V_o) defective TiO_2 oriented (100) and (110) planes, yielding four different $SnSe_2$/TiO_2 structures. An atomistic representation of the (100) and (110) defect-free structures is reported in Fig. 8a,b, while those corresponding to defective (100) and (110) TiO_2 are shown in Supplementary Information Fig. S11. We found lattice mismatches of 4.8% and of 3.2% corresponding to the (100) and (110) oriented heterostructures, yielding modest and negative (around 10–20 mJ m^{-2}) associated formation energies, consistent with those typical of physiosorbed 2D-oxide layers[52]. These results indicate a weakly exothermic, van der Waals contact between 2D-$SnSe_2$ and TiO_2, which maintains their individual phase structures.

Bandgap structure of $SnSe_2$/TiO_2

The left (blue) and right (pink) panels of Fig. 8c,d show the band alignment of defect-free and defective (100) and (110) TiO_2 planes. The projected densities of states (DOS) of these structures are provided in Supplementary Information Figs. S12,13. For both (100) and (110) planes, the defect-free interfaces Fig. 7c,d (blue), display a wide, clean band gap for TiO_2 and a narrower one for $SnSe_2$. Both defect-free (100) and (110) planes of the $SnSe_2$/TiO_2 heterostructure exhibit a type-I (straddling) alignment[53], indicating that the $SnSe_2$ band edges lie entirely within the TiO_2 gap. Corresponding to this configuration, electrons and holes are confined in $SnSe_2$, while TiO_2 acts as a potential barrier. In the case of defective (100) TiO_2 plane (Fig. 8c—pink), the defect levels strongly push the Fermi level close to the conduction band, reducing the effective barrier height for electron transfer.

Table 2 | 0 K adsorption energies for H^+, OH^-, $\frac{1}{2}O_2$ and H_2O on different TiO_2 surfaces

Adsorption Energies E_{ads} (eV)				
Crystallographic Planes	H^+	$\frac{1}{2}O_2$	OH^-	H_2O
(100)	0.45	−0.13	−1.29	−0.86
Defective (100)	−0.41	−4.74	−5.02	−0.34
Defective (110)	−0.57	−4.05	−5.42	−2.52

Negative values refer to exothermic adsorption.

Opposedly, in the case of (110) plane (Fig. 8d—pink), the vacancy level lies within the TiO_2 conduction band, producing a shallow donor/accumulation behaviour in TiO_2. As a result, the conduction band of TiO_2 shifts downward relative to that of $SnSe_2$, establishing a S-Scheme band alignment, consistent with the S-scheme model of Fig. 5b based on experimental measurements of Fermi Level (FL), valence band (VB) and conduction band (CB).

Oxygen evolution reaction (OER) thermodynamics on $SnSe_2$/TiO_2 heterostructure

We preliminary calculated (see Supplementary Information Section S5.4) 0 K adsorption energies of H^+, OH^-, $\frac{1}{2}O_2$ and H_2O on defect-free (100) and defective (100) and (110) TiO_2 planes, as reported in Table 2. On TiO_2/$SnSe_2$, water adsorbs via heterolytic splitting to Ti–OH and O–H; although the dissociated state is favoured on both (100) and (110), only (110) is characterized by the right combination of geometry and local electrostatics that lower the kinetic barrier triggering spontaneous dissociation. It turns out that adsorption energies on defective (100) and (110) TiO_2 are all exothermic, yielding the highest energetic contribution corresponding to OH^- adsorption, if compared to H^+, $\frac{1}{2}O_2$ and H_2O, respectively. Adsorption energies on defect-free TiO_2 (100) are all exothermic excluding H^+, however, significantly smaller than adsorption energies calculated for defective

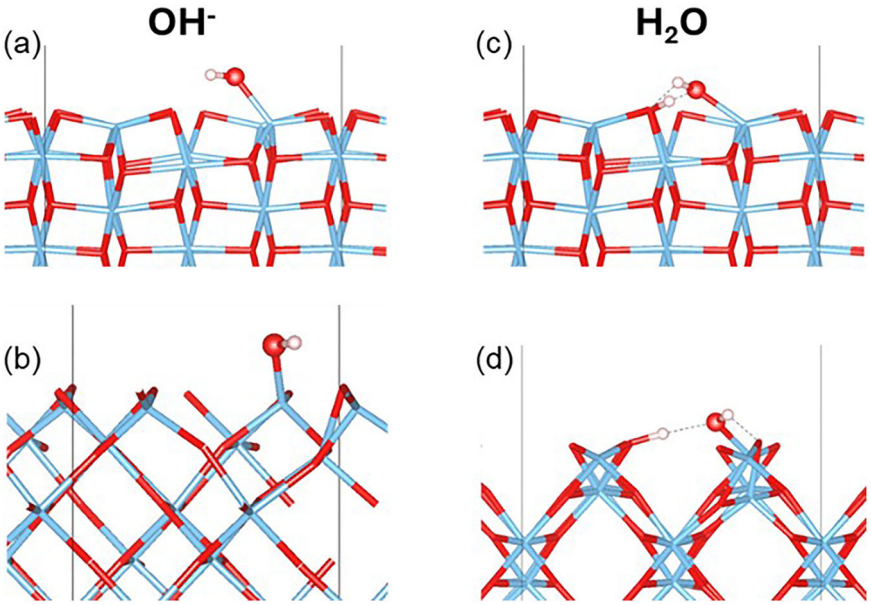


Fig. 9 | Optimized adsorption molecular configurations over oxygen defective (110) TiO_2 surface. Adsorption configuration geometries of (**a**, **b**) OH^- (yz and xz plane views) and (**c**, **d**) H_2O (yz and xz plane views) molecules over oxygen defective (110) TiO_2 surface.

TiO_2. These preliminary findings suggest that oxygen-defective TiO_2: (i) induce defect states within the band gap (Fig. 8c,d—pink), (ii) enhance molecular adsorption in the order $OH^- > \frac{1}{2}O_2 > H_2O > H^+$, and (iii) make the defective (110) and (110) TiO_2 planes more favourable than defect-free (100) TiO_2 plane to OH^- adsorption compared to $\frac{1}{2}O_2$, H_2O and H^+.

The optimized adsorption molecular configurations of OH^- and H_2O of defective (110) TiO_2, are shown in Fig. 9. A complete picture of all adsorption configurations of H^+, OH^-, $\frac{1}{2}O_2$ and H_2O on (110) and (100) defective TiO_2 is provided in Supplementary Information Figs. S14,15. Accordingly, H_2O adsorption proceeds via a dissociative chemisorption pathway (Fig. 9c,d), resulting in the formation of OH^- and H^+, over defective surface-oxygen (110) TiO_2.

Free energy diagrams of the OER reaction steps on 2D-$SnSe_2$/TiO_2 heterostructure

We completed the DFT computations on defective (100) and (110) $SnSe_2$/TiO_2 by evaluating the OER thermodynamics according to the four reaction steps here reported (reactions in Eqs. 7–10):

$$OH^- + * \rightarrow OH^* + e^- \quad (7)$$

$$OH^* + OH^- \rightarrow O^* + H_2O_{(l)} + e^- \quad (8)$$

$$O^* + OH^- \rightarrow OOH^* + e^- \quad (9)$$

$$OOH^* + OH^- \rightarrow * + O_{2(g)} + H_2O_{(l)} + e^- \quad (10)$$

where * refer to the active site, and OH*, O*, and OOH* are adsorbed intermediates on the TiO_2 surface[54,55]. Notably, we utilized the computational hydrogen electrode (CHE) approach (i.e., referencing the H^+/e^- chemical potential to ½H_2 and shifting step energies by eU at a chosen potential and pH), as introduced by Nørskov[56], which is widely adopted for mechanistic analysis of OER evolution on oxide surfaces[57]. Complete formulas for ΔG(U,pH), reference states, and all numerical corrections are given in section "Methods: Computational Model".

The free energy diagrams for (100) and (110) defective TiO_2 planes are shown in Fig. 8e,f. Regarding defective (100), the non-biased energy diagram (Fig. 8e—red line) highlights that the Potential Determining Step (PDS), defined as the step associated with the highest reaction free energy [eV] difference, is O* → OOH*, corresponding to the shaded grey region of (Fig. 8e). This result is consistent with the high energy required to form O–O bonds in metal oxides[58], corresponding to Eq. 9. However, under Linear Sweep Voltammetry (LSV) operational conditions (Fig. 3), the photoanode is subjected to a potential sweep between 0.2 and 1.7 V vs RHE (Fig. 3c), which substantially changes the energetics of the OER as respect to non-polarized conditions (i.e. Figure 8e—red-line). For this purpose, we extended the DFT OER free energy calculations of over defective (100) TiO_2 plane by simulating an applied potential bias, here indicated as U [V vs CHE] in the 0.00 and 2.40 V range. We found (Fig. 8e—blue line) that a minimum overpotential of η = 1.17 V, corresponding to U = 2.40 V vs CHE, where η = U – E_{OER} (with E_{OER} = 1.23 V vs CHE being the OER theoretical potential), is required to offset the O* → OOH* potential determining step (PDS) and render all the other reaction steps exothermic (i.e. <0 eV). DFT calculations on non-biased defective (110) plane (Fig. 8f – red line), exhibit OH* → O* as the PDS, corresponding to the shaded grey region of (Fig. 8f), consistent with previous DFT calculations[58,59]. Accordingly, DFT free energy calculations of (110) TiO_2 plane under an applied potential bias (Fig. 8f—blue line) yield an overpotential of η = 0.67 V (i.e. U = 1.90 V vs CHE) to offset the potential determining step (PDS) and render all reaction steps ≤ 0 eV. The overpotential of η = 0.67 V of defective (110) TiO_2, compared to η = 1.17 V of defective (100) TiO_2 plane, indicate that defective (110) TiO_2 plane thermodynamically favour the OER.

In conclusion, DFT theoretical computations highlight that: the band-structure of defective (110) $SnSe_2$/TiO_2 (Fig. 8d—pink) matches an S-scheme mechanism which has been experimentally inferred from XPS, Mott-Schottky and Bandgap measurements, as shown in Fig. 6, and yields a higher affinity towards OH^- than the (100) surface, according to adsorption energies of Table 2. Remarkably, the defective (110) TiO_2 plane well conveys the main microstructural features of our sol-gel prepared films considering the prevalent crystallographic orientation (Fig. 1g) and the defective stoichiometry observed by XPS (Fig. 1l), anchoring the DFT model to the experimental evidence.

Discussion

In summary, we have shown that layered 2D-$SnSe_2$ nanosheets grown on ordered mesoporous TiO_2 thin films constitute a stable photoanode for the oxygen evolution reaction (OER) under neutral-pH conditions. The solvothermal growth route yields a uniform and strongly adhered 2D-$SnSe_2$/TiO_2 heterointerface, where the mesoporous TiO_2 offers a high surface area and structurally defined nucleation sites, promoting the growth of well-oriented 2D-$SnSe_2$ nanoplatelets.

Compared with bare TiO_2, the 2D-$SnSe_2$/TiO_2 photoanode presents improved visible-light absorption and an ~16-fold enhanced photoelectrochemical (PEC) OER response, reaching 0.80 mA cm^{-2} at 1.7 V vs RHE under simulated solar illumination. Chronoamperometry tests, performed over 3 × 16 h irradiation cycles, indicate an overall photocurrent decay below 3%, while post-test SEM/EDX and Raman analyses further support the retention of morphology and chemical composition under operational conditions. However, quantitative O_2 evolution and Faradaic efficiency measurements remain necessary to unambiguously quantify the OER output, and the stability assessment should be extended above the reported 48 h timeframe to be relevant in benchmarked PEC applications.

By combining experimental and DFT theoretical computations with XPS, Mott–Schottky, and optical bandgap measurements, an S-scheme OER mechanism over the oxygen-defective (110) TiO_2 plane of the 2D-$SnSe_2$/TiO_2 heterostructure is proposed. As an additional proof of the proposed mechanism, LSV test utilizing methanol confirmed photoanode holes (h^+) to be the photoinduced charges participating to the oxygen evolution, eventually corroborating the S-Scheme mechanism. Moreover, the calculated differential adsorption free energies for the four OER intermediates on oxygen-defective TiO_2 (110) identified OH* → O* as the potential-determining OER step. Notably, the proposed S-scheme charge-transfer mechanism is further supported by the measured decrease in SO_4^{2-} concentration during PEC operation (consistent with an electron-consumption pathway involving sulphate ions) and by the photocurrent increase observed in hole-scavenging tests with methanol. Nevertheless, additional operando or time-resolved evidence of interfacial charge-transfer kinetics would provide even stronger support for this charge transfer mechanism.

Overall, coupling TiO_2 with a visible-light-responsive 2D-$SnSe_2$ co-catalyst to yield a 2D-$SnSe_2$/TiO_2 heterostructure provides a practical route toward an efficient and stable PEC OER photoanode in neutral electrolytes. Ultimately, the 2D-$SnSe_2$/TiO_2 heterostructure presented here contributes to broadening the applicability of group-IV chalcogenides MX_2 (M = Sn, Ge; X = S, Se, Te)/TiO_2 heterojunctions for practical PEC devices.

Methods

Mesoporous titania (TiO_2) thin film deposition over FTO glass substrates

Fluorine-doped Tin Oxide (FTO, SnO_2:F) coated glass substrates with 2.1 mm thickness and 50 × 25 mm size (Sigma-Aldrich, Cod: 735159) were cleaned by ultrasonic bath for 10 min (Elmasonic P 60 H working at 37 kHz and 100% power) with sequential baths of Acetone (Sigma-Aldrich, Cas Nr: 67-64-1), distilled water and Ethanol (Sigma-Aldrich, Cas Nr: 64-17-5) and left to dry in air. Mesoporous Titania—TiO_2 thin films were grown on FTO substrates by the following procedure: 1.6 cm^3 (0.014 mol) of $TiCl_4$ (Sigma-Aldrich, Cas nr: 7550-45-0) were mixed by stirring in 8.4 cm^3 (0.14 mol) of ethanol to give solution A. In another vial, 0.138 g ($1.03*10^{-5}$ mol) of Pluronic F127 (Sigma-Aldrich, Cas Nr: 9003-11-6) was dissolved in 7.35 cm^3 of ethanol (0.126 mol) to give solution B. Then, 1.47 cm^3 of solution A was added to solution B and the mixture stirred for 5 min. Afterwards, 0.588 cm^3 (0.03 mol) of milli-Q water were added, stirring the final solution for 2 h at room temperature in a closed vial[35]. TiO_2 thin films were obtained by dip-coating 35 mm of the total substrate's height for 30 s and then withdrawing at a speed of 10 cm/min. The conditions inside the deposition chamber have been kept at 25 °C temperature and 21-23% relative humidity (RH%). After dip-coating, each sample was dried in oven in static air at 60 °C for 15 min and then annealed in static air at 400 °C for 3 h.

Solvothermal growth of 2D-$SnSe_2$ platelets over mesoporous TiO_2 thin films

Two different routes have been employed to synthesize 2D-$SnSe_2$ over TiO_2 coated FTO substrates, here described.

Route 1: 0.115 g (0.5 mmol) of $SnCl_2*2H_2O$ (Sigma-Aldrich, Cas Nr: 10025-69-1) were dissolved by stirring for 30 min in 20 ml of distilled water (Sigma Aldrich, Cas Nr: 112-80-1). Subsequently, 0.111 g (1 mmol) of SeO_2 (Sigma Aldrich, Cas Nr: 7446-08-4) were added and the solution stirred for another 30 min. Finally, 2 ml of $N_2H_4*2H_2O$ (Sigma Aldrich, Cas Nr: 10217-52-4) was added to the reactants and the 50 mL volume PTFE reactor chamber sealed. The hydrothermal reactor was heated using a laboratory oven (ISCO 9000), with a rate of 5 °C/min from 25 to 180 °C. After 24 h at 180 °C, the reactor was left to cool naturally[23].

Route 2: 0.115 g (0.5 mmol) of $SnCl_2*2H_2O$ (Sigma-Aldrich, Cas Nr: 10025-69-1) were dispersed by stirring for 30 min in 20 ml of Oleic Acid (Sigma Aldrich, Cas Nr: 112-80-1). Afterwards, 0.090 g (1 mmol) of Se powder (Sigma Aldrich, Cas Nr: 7782-49-2) were added and stirred for another 30 min. The obtained dispersion was poured in a 50 ml hydrothermal reactor and then heated with a rate of 5 °C/min from 25 to 220 °C, using a laboratory oven (ISCO 9000)[24]. After 24 h at 220 °C, the reactor was left to cool naturally. To grow $SnSe_2$ over TiO_2 coated FTO glass substrates, the latter have been placed into the reactor with the conductive side facing upwards. The obtained sample were substrates covered with a black film. After processing, the products have been washed carefully several times with acetone and ethanol and then left to dry in air.

Morphological and optical characterization

Scanning electron microscopy (SEM) and Energy dispersive X-ray chemical maps (EDX) were recorded by mounting the 2D-$SnSe_2$ and 2D-$SnSe_2$/TiO_2 samples with the conductive side upwards on a metallic sample holder, ensuring electric contact with a copper tape, using a Gemini FE-SEM 500 (Carl Zeiss AG, Germany) working at an accelerating voltage of 5 kV. The statistical analysis of 2D-$SnSe_2$ flakes lateral sizes was based on approximately 100 flakes from three SEM images acquired in different substrate areas. The optical properties (absorbance and reflectance spectra) were measured using a PerkinElmer Lambda 1050 + UV/vis/NIR spectrophotometer (PerkinElmer Inc., Waltham, USA) equipped with a 100 mm integrating sphere. XPS spectra were obtained using a PHI 1257 spectrometer equipped with monochromatic Al Kα source (hν = 1486.6 eV) and operating at a spectral resolution of 250 meV, depositing the TiO_2 and 2D-$SnSe_2$ samples over *p*-type Si substrates. Grazing Incidence X-Ray Diffraction (GI-XRD) was performed by XRD-PAN Analytical X'PERT Pro using Cu Kα1 radiation (λ = 1.5406 Å) in parallel geometry, with an incident angle of 0.8°. Atomic force microscopy (AFM) was performed using an NT-MDT Ntegra microscope in semi-contact mode at a scan speed of 0.05 Hz. A silicon tip with a typical resonance frequency of 252 kHz, a force constant of 11.8 N/m, and a curvature radius of 10 nm was used. The statistical analysis of 2D-$SnSe_2$ flakes thicknesses was based on 10 AFM images acquired over scanned areas of 110 μm × 110 μm. Raman measurements were carried out using a Bruker Senterra confocal Raman microscope equipped with a 532 nm excitation laser operated at a nominal power of 5 mW and a 100x objective lens. Spectra were acquired in the 60–1560 cm^{-1} range with a spectral resolution of 5 cm^{-1}, using an integration time of 30 s and averaging over 4 accumulations.

Photoelectrochemical characterization

All the photoelectrochemical characterization has been performed in a home-built photoelectrochemical (PEC) cell. The electrolyte for all tests was Na_2SO_4 (Sigma Aldrich, CAS 7757-82-6) solution 0.5 M in distilled water (pH ~ 7). The electrolyte used for hole scavenging tests was a 10% vol/vol solution of the previous 0.5 M Na_2SO_4 solution in distilled water and methanol (Sigma Aldrich, CAS 67-56-1). The working electrode area immersed in the electrolyte was 7.5 cm^2. All the current densities [mA/cm^2] were calculated referring to the photoelectrode's immersed area of 7.5 cm^2. The counter electrode (CE) and the reference electrode (RE) were respectively a Platinum (Pt) foil (Thermo Fisher Scientific, CAS 7440-06-4) of 50*5 mm dimensions and 0.1 mm thickness and an Ag/AgCl saturated KCl electrode (Xylem Analytics, Germany) with a standard potential of $E^0_{Ag/AgCl}$ = 0.197 V vs SHE. The measured potentials were converted to the Reversible Hydrogen Electrode (RHE) scale according to Eq. 10

$$V(\text{vs RHE}) = V(\text{vs Ag/AgCl}) + E^0_{Ag/AgCl} + 0.059 * \text{pH} \quad (10)$$

A Parstat 4000 A (Ametek Scientific Instruments, USA) Potentiostat-Galvanostat coupled with a PC running the VersaStudio 2.65.2 software was used to acquire the data. Linear Sweep Voltammetry (LSV) curves under dark and illuminated conditions were performed from 0.2 to 1.7 V vs RHE at a scan rate of 200 mV/s. Chopped light Chronoamperometry (CA) using the Xe lamp and UV light was acquired by keeping the WE at a constant potential of 1.7 V vs RHE within a timeframe of 300 s and by chopping light every 10 seconds. Three repeated long-term Chronoamperometric tests (CA) under solar-light illumination, each with a duration of 16 h, were performed by keeping the WE at a constant potential of 1.7 V vs RHE. Each test was performed on freshly prepared Na_2SO_4 0.5 M electrolyte. The concentration of SO_4^{2-} anions as a function of reaction time ($[SO_4^{2-}]_0$ = 71.01 g/L) was quantified by Ion Chromatography (IC, Dionex ICS-5000 +) after calibration. Specifically, at reaction times of 0, 4, 8, 12 and 16 h, 1 mL aliquots of the electrolyte were sampled. A two-step dilution (total 1:500) was performed: 1.00 mL stock solution diluted to 500.00 mL (142.0 ppm intermediate), then 3.52 mL intermediate to 100.00 mL (50 ppm working solution). Samples were filtered (0.45 µm nylon membranes, Whatman, Sigma Aldrich, Code: WHA7404004) prior to injection. Unless otherwise indicated, all the potentials in the text refer to the RHE scale. Mott-Schottky (MS) curves of TiO_2 and 2D-$SnSe_2$ on FTO substrates in Na_2SO_4 0.5 M electrolyte are obtained from impedance measurements at 10^3 Hz frequency using potentials from −0.5 to 1.0 V vs SHE. The working electrode (WE) was irradiated using UV (M365L4), Blue (M470L4), Green (M530L4) and Red (M625L4) monochromatic LEDs (Thorlabs, Germany) with wavelengths of 365, 470, 530 and 625 nm, respectively, equipped with collimating lenses (SM1U25-A, Thorlabs). The light intensity emitted from the LEDs was calibrated to deliver a constant irradiance of 250 µW/mm^2 to the working electrode (WE) surface. Specifically, the irradiance was measured with a photodetector (S405C, Thorlabs) connected to an optical energy meter (PM100D, Thorlabs) and positioned instead of the WE. The LEDs output was regulated using a voltage generator (PS2520G, Tektronix)-controlled LED driver (LEDD1B, Thorlabs). Solar light illumination has been simulated using a 300 W Xenon solar simulator (LS0306, Quantum Design) equipped with an AM 1.5 G filter, calibrated to deliver an irradiance of 1000 µW/mm^2 (1 sun) to the electrode surface. With the aim of studying the stability of the electrodes to the testing conditions and to offset any effect deriving from sequential LSV scans, the LSV curves sequence has been kept always as the following: dark, solar light, Red, Green, Purple Blue and UV lights.

Measure of $[SO_4^{2-}]$ as a function of reaction time

Three repeated long-term Chronoamperometric tests (CA) under solar-light illumination, each with a duration of 16 h, were performed by keeping the WE at a constant potential of 1.7 V vs RHE. Each test was performed on freshly prepared Na_2SO_4 0.5 M electrolyte. The concentration of SO_4^{2-} anions as a function of reaction time ($[SO_4^{2-}]_0$ = 71.01 g/L) was quantified by Ion Chromatography (IC, Dionex ICS-5000 +) after calibration. Specifically, at reaction times of 0, 4, 8, 12 and 16 h 1 mL aliquots of the electrolyte were sampled. A two-step dilution (total 1:500) was performed: 1.00 mL stock solution diluted to 500.0 mL (142.0 ppm intermediate), then 3.52 mL intermediate to 100.0 mL (50 ppm working solution). Samples were filtered (0.45 µm PTFE membranes) prior to injection.

Computational model

Reference DFT simulations were performed within the framework of Density Functional Theory (DFT), using the Vienna Ab initio Simulation Package (VASP)[60–62] under periodic boundary conditions, employing the projector augmented wave (PAW) method[63,64]. The Perdew-Burke-Ernzerhof revised for solids (PBEsol) exchange-correlation functional[65] was employed. Partial occupancies of the electronic states were set using fourth-order Methfessel-Paxton smearing[66] with a width of 0.05 eV. Converged energies for the bulk systems were achieved with a plane-wave energy cutoff of 600 eV and a self-consistent field (SCF) convergence criterion of 10^{-8} eV. The force convergence tolerance was set to 0.01 eV/Å for each atom in all directions. A k-point Monkhorst-Pack mesh sampling of the Brillouin zone[67] was employed: for bulk anatase, a 13 × 13 × 5 mesh was considered, while an 18 × 18 × 8 mesh was used for bulk $SnSe_2$. For the slabs, a 4 × 4 × 1 mesh was used for all slabs, either pristine (TiO_2, $SnSe_2$) or heterostructured (TiO_2 + $SnSe_2$). Specifically, the $SnSe_2/TiO_2$ heterostructures are composed of three TiO_2 layers and two $SnSe_2$ layers.

We estimated reaction free energies for electrochemical steps from our DFT adsorption energies by treating the proton–electron pair as a single reservoir, the computational hydrogen electrode (CHE) the chemical potential of a ($H^+ + e^-$) pair at pH 0 equals ½ the chemical potential of $H_{2(g)}$ at the same T and P, and an applied potential U simply shifts the electron chemical potential by -eU, as introduced by Nørskov et al.[56]. This allowed us to build Gibbs free energies for each elementary OER step without modeling explicit solvated protons/electrons. The four OER steps are explicitly reported in the main text, section "Results": "Free energy diagrams of the OER reaction steps on 2D-$SnSe_2/TiO_2$ heterostructure". We follow the alkaline four-step sequence and evaluate ΔG for each step at T = 298.15 K and 1 atm within CHE.

For every elementary step i we use the standard CHE expression of Eq. 11

$$\Delta G_i = \Delta E_i + \Delta EZPE - T\Delta S_i - n_i eU + \Delta G_i, pH \quad (11)$$

where:

- ΔE_i are the DFT adsorption energies for OH*, O*, and O_2* at T = 0 K;
- $\Delta EZPE—T\Delta S_i$ are the vibrational zero-point and entropic corrections for adsorbed species. These are usually computed by performing finite difference calculation and considering the configurational entropy on the surface (coverage randomness). In our work, instead, we provide a reasonable estimate of an uncertainty resulting from not calculating these terms explicitly. In the classic CHE formulation, Nørskov/Rossmeisl tabulate ΔZPE—TΔS for ORR/OER-like steps[56];
- or forming OH* from * + H_2O—½H_2 the correction is ≈ +0.35 eV;
- for O*-related steps it's ≈ 0.05 eV;
  The entropy term is typically large for gas molecules and small for adsorbates. From NIST
- $H_{2(g)}$ standard molar entropy (gas, 1 bar) 130.680 J/(molK);
- $H_2O_{(l)}$ standard molar entropy (liquid, 1 bar) 69.95 J/(molK);
  With these numbers for ΔGTΔS, with T = 298.15 K, we get -0.404 eV for H_2 and -0.216 eV for H_2O, providing an upper bound value for these steps. Following these considerations, we decide to bracket each step with a ± 0.4 eV band that covers reasonable ranges for ΔEZPE -$T\Delta S_i$ uncertainties when full phonons are not recomputed on every configuration. (This magnitude matches the canonical CHE literature for OH*/O*/OOH* steps[68,69].)
- $n_i eU$ is the electrical work term for an electrochemical step transferring n electrons = -neU. In the 4-step OER, each step carries one electron n = 1 every time; shifting the whole step down by U eV at potential U;
- ΔG_i,pH is the pH correction from the Nernst relation, i.e. free-energy shift due to the chemical potential of protons at a given pH, which equals to mkBT ln 10 x pH. At 298.15 K, kBTln10 ≈ 0.05916 eV per proton per pH unit. In our calculations we set pH = 0;

We then compute ΔG_i directly considering our adsorption energetics. However, the OOH* term is estimated via the established OOH*–OH* scaling ($\Delta G_{OOH^*} \approx \Delta G_{OH^*} + 3.2 \pm 0.2$ eV). In fact, across oxides and metals, DFT shows a near-constant offset between OOH* and OH* adsorption free energies: this OOH–OH scaling was established for OER/ORR and used to build activity volcano plots[70]. The OOH* moiety can be viewed as OH* plus formation of an O–O bond and a bound H; as long as the same kind of site binds both species, the extra binding/strain/solvation contributions are similar across materials, yielding an almost constant offset c. This relation has a slope of ~1 and the intercept near 3.2 eV in large DFT datasets[71,72]. The typical uncertainty when OOH* is not computed explicitly

is typically set at 0.2 eV[70,73]. Furthermore, it was proven that the relation is functional-independent, reinforcing its robustness across common GGAs[74]. Gas-phase $O_{2(g)}$ is treated explicitly in step 4 (see Eq. 10). We plot cumulative $\sum k \le i\ \Delta G_k(U)$ along Eq. 12

$$* \rightarrow OH^* \rightarrow O^* \rightarrow OOH^* \rightarrow O_{2(g)} \quad (12)$$

The potential-determining step (PDS) is the largest uphill at U = 0; its height gives the limiting potential U_{lim}, and the theoretical overpotential is $\eta = U_{lim} - 1.23$ V, where 1.23 V is the thermodynamic equilibrium potential for splitting liquid water at 298 K, 1 bar. Because of the above-introduced approximations, we treat η as a mechanistic descriptor (identify PDS; compare facets/defects), not a point-prediction of device voltage.

Data availability

All relevant data to this study are shown in the article and its supplementary information files.

Received: 18 February 2026; Accepted: 24 June 2026;
Published online: 15 July 2026

References

1. Zhao, Y. et al. Recent advancements in photoelectrochemical water splitting for hydrogen production. *Electrochem. Energy Rev*. **6**, 14 (2023).
2. Xie, X. et al. Oxygen evolution reaction in alkaline environment: material challenges and solutions. *Adv. Funct. Mater*. **32**, 2110036 (2022).
3. Dong, G., Yan, L. & Bi, Y. Advanced oxygen evolution reaction catalysts for solar-driven photoelectrochemical water splitting. *J. Mater. Chem. A Mater.* **11**, 3888–3903 (2023).
4. Gao, R. et al. Towards long-term photostability of nickel hydroxide/bivo4 photoanodes for oxygen evolution catalysts via in situ catalyst tuning. *Angew. Chem.* **132**, 6272–6277 (2020).
5. Roger, I., Shipman, M. A. & Symes, M. D. Earth-abundant catalysts for electrochemical and photoelectrochemical water splitting. *Nat. Rev. Chem*. **1**, 0003 (2017).
6. Burke, M. S., Enman, L. J., Batchellor, A. S., Zou, S. & Boettcher, S. W. Oxygen evolution reaction electrocatalysis on transition metal oxides and (oxy)hydroxides: activity trends and design principles. *Chem. Mater.* **27**, 7549–7558 (2015).
7. Song, Y. et al. Electronic structure tuning of 2D metal (hydr)oxides nanosheets for electrocatalysis. *Small* **17**, 2002240 (2021).
8. Fareza, A. R., Nugroho, F. A. A., Abdi, F. F. & Fauzia, V. Nanoscale metal oxides-2D materials heterostructures for photoelectrochemical water splitting—a review. *J. Mater. Chem. A Mater.* **10**, 8656–8686 (2022).
9. Moon, C., Seger, B., Vesborg, P. C. K., Hansen, O. & Chorkendorff, I. Wireless photoelectrochemical water splitting using triple-junction solar cell protected by TiO_2. *Cell Rep. Phys. Sci*. **1**, 100261 (2020).
10. Wilson, H. et al. Photocorrosion of n- and p-type semiconducting oxide-covered metals: case studies of anodized titanium and copper. *Phys. Status Solidi A*. **219**, 2100852 (2022).
11. Tamaki, Y. et al. Dynamics of efficient electron-hole separation in TiO_2 nanoparticles revealed by femtosecond transient absorption spectroscopy under the weak-excitation condition. *Phys. Chem. Chem. Phys.* **9**, 1453–1460 (2007).
12. Robertson, J. Electronic structure of SnS_2, $SnSe_2$, CdI_2, and PbI_2. *J. Phys. C: Solid State Phys*. **12**, 4753–4765 (1979).
13. Huang, Y., Sutter, E., Parkinson, B. A. & Sutter, P. High mobility, high carrier density SnSe2 field-effect transistors with ultralow subthreshold swing and gate-controlled photoconductance switching. *Adv. Electron. Mater*. **11**, 2400691 (2025).
14. D'Olimpio, G. et al. Charge redistribution mechanisms in $SnSe_2$ surfaces exposed to oxidative and humid environments and their related influence on chemical sensing. *J. Phys. Chem. Lett.* **11**, 9003–9011 (2020).
15. De Santis, J. et al. Bidimensional $SnSe_2$—mesoporous ordered titania heterostructures for photocatalytically activated anti-fingerprint optically transparent layers. *Nanomaterials* **13**, 1406 (2023).
16. Tang, H. et al. Enhancing photocatalytic performance by one-step vapor deposition of SnSe/$SnSe_2$ composites. *ACS Appl. Energy Mater.* **8**, 13831–13839 (2025).
17. Christoforidis, K. C., Sengele, A., Keller, V. & Keller, N. Single-step synthesis of SnS_2 nanosheet-decorated TiO_2 anatase nanofibers as efficient photocatalysts for the degradation of gas-phase diethylsulfide. *ACS Appl. Mater. Interfaces* **7**, 19324–19334 (2015).
18. Zhang, J. et al. Anatase TiO_2 nanosheets with coexposed {101} and {001} facets coupled with ultrathin SnS_2 nanosheets as a face-to-face *n-p-n* dual heterojunction photocatalyst for enhancing photocatalytic activity. *Appl. Surf. Sci.* **420**, 839–848 (2017).
19. Sun, L. et al. Role of SnS_2 in 2D-2D SnS_2/TiO_2 nanosheet heterojunctions for photocatalytic hydrogen evolution. *ACS Appl. Nano Mater.* **2**, 2144–2151 (2019).
20. Mu, J. et al. Enhanced light trapping and high charge transmission capacities of novel structures for efficient photoelectrochemical water splitting. *Nanoscale* **10**, 11881–11893 (2018).
21. Innocenzi, P. & Malfatti, L. Mesoporous ordered titania films: an advanced platform for photocatalysis. *J. Photochem. Photobiol. C: Photochem. Rev*. **58,** 100646 (2024).
22. Innocenzi, P. Mesoporous ordered films via self-assembly: trends and perspectives. *Chem. Sci*. **116,** 13264–13279 (2022).
23. Liu, K., Liu, H., Wang, J. & Feng, L. Synthesis and characterization of $SnSe_2$ hexagonal nanoflakes. *Mater. Lett.* **63**, 512–514 (2009).
24. Rai, R. K. et al. Morphology controlled synthesis of low bandgap $SnSe_2$ with high photodetectivity. *Nanoscale* **11**, 870–877 (2019).
25. Ma, D. W. & Cheng, C. Synthesis of $SnSe_2$ nanorods and nanoplates by an organic solution-phase route. *J. Nanosci. Nanotechnol.* **13**, 4433–4436 (2013).
26. Lu, C. et al. Direct Z-Scheme $SnSe_2$/SnSe Heterostructure Passivated by Al_2O_3 for Highly Stable and Sensitive Photoelectrochemical Photodetectors. *ACS Appl. Mater. Interfaces* **15**, 6156–6168 (2023).
27. Saha, S., Banik, A. & Biswas, K. Few-layer nanosheets of n-type $SnSe_2$. *Chem. Eur. J. I* **22**, 15634–15638 (2016).
28. Paolucci, V. et al. Bidimensional engineered amorphous *a*-SnO_2 interfaces: synthesis and gas sensing response to H_2S and humidity. *ACS Sens.* **7**, 2058–2068 (2022).
29. Zheng, Q., Cheng, X. & Li, H. Microwave synthesis of high activity $FeSe_2$/*C* catalyst toward oxygen reduction reaction. *Catalysts* **5**, 1079–1091 (2015).
30. Idriss, H. On the wrong assignment of the XPS O1s signal at 531–532 eV attributed to oxygen vacancies in photo- and electro-catalysts for water splitting and other materials applications. *Surf. Sci*. **712**, 121894 (2021).
31. Badrinarayanan, S., Mandale, A. B., Gunjikar, V. G. & Sinha, A. P. B. Mechanism of high-temperature oxidation of tin selenide. *J. Mater. Sci*., **21,** 3333–3338 (1986).
32. Moulder, J. F., Stickle, W. F., Sobol, P. E. & Bomben, K. D. Handbook of X-Ray Photoelectron Spectroscopy (ed. Chastain, J.) (Perkin-Elmer Corporation, 1992).
33. Wang, J., Mueller, D. N. & Crumlin, E. J. Recommended strategies for quantifying oxygen vacancies with X-ray photoelectron spectroscopy. *J. Eur. Ceram. Soc*. **44**, 116709 (2024).
34. Lee, J. et al. Phase-selective active sites on ordered/disordered titanium dioxide enable exceptional photocatalytic ammonia synthesis. *Chem. Sci.* **12**, 9619–9629 (2021).
35. Herrera, F. C. et al. Chemical design of efficient photoelectrodes by heterogeneous nucleation of carbon dots in mesoporous ordered titania films. *Chem. Mater.* **35**, 8009–8019 (2023).

36. Mukhokosi, E. P., Krupanidhi, S. B. & Nanda, K. K. Band gap engineering of hexagonal $SnSe_2$ nanostructured thin films for infra-red photodetection. *Sci. Rep*. **7**, 15215 (2017).
37. Makuła, P., Pacia, M. & Macyk, W. How to correctly determine the band gap energy of modified semiconductor photocatalysts based on UV-Vis spectra. *J. Phys. Chem. Lett.* **9**, 6814–6817 (2018).
38. Khan, M. I., Bhatti, K. A., Qindeel, R., Althobaiti, H. S. & Alonizan, N. Structural, electrical and optical properties of multilayer TiO_2 thin films deposited by sol–gel spin coating. *Results Phys.* **7**, 1437–1439 (2017).
39. Shen, C. et al. Atomic layer deposition of MoS_2 decorated TiO_2 nanotubes for photoelectrochemical water splitting. *Adv. Mater. Interfaces* **9**, 2200643 (2022).
40. Singh, B. et al. $PtSe_2/TiO_2$ nanotubes heterostructure for enhanced photoelectrochemical water splitting. *J. Mater. Sci.* **59**, 15201–15220 (2024).
41. Lin, J. et al. SnS_2 nanosheets/H-TiO_2 nanotube arrays as a type II heterojunctioned photoanode for photoelectrochemical water splitting. *ChemSusChem* **12**, 961–967 (2019).
42. Gelderman, K., Lee, L. & Donne, S. W. Flat-band potential of a semiconductor: using the Mott-Schottky equation. *J. Chem. Educ*. **84**, 685–688 (2007).
43. Liu, X. et al. In-situ construction of S-scheme $SnSe_2$/Se heterojunction photocathode with enhanced photoelectrochemical performance by a facile one-step CVD process. *J. Alloys Compd*. **960**, 37 (2023).
44. Peng, W., Yang, C. & Yu, J. Bi_2O_3 and g-C_3N_4 quantum dot modified anatase TiO_2 heterojunction system for degradation of dyes under sunlight irradiation. *RSC Adv.* **10**, 1181–1190 (2019).
45. Hu, Y. et al. $BiVO_4/TiO_2$ nanocrystalline heterostructure: a wide spectrum responsive photocatalyst towards the highly efficient decomposition of gaseous benzene. *Appl. Catal. B* **104**, 30–36 (2011).
46. Zhong, Y., Zhang, L., Chen, W. & Zhu, H. Macro van der Waals p-n heterojunction based on SnSe and $SnSe_2$. *Nanotechnology* **31**, 385203 (2020).
47. Streetman, B. G. & Sanjay, B. K. Solid state electronic devices. (Pearson Education Limited, 2016).
48. Mesa, C. A. et al. Kinetics of photoelectrochemical oxidation of methanol on hematite photoanodes. *J. Am. Chem. Soc.* **139**, 11537–11543 (2017).
49. Sultana, S., Darowska, I., Pisarek, M., Sulka, G. D. & Syrek, K. Designing TiO_2 nanotubular arrays with Au-CoO_x core-shell nanoparticles for enhanced photoelectrochemical methanol and lignin oxidation. *ACS Appl. Mater. Interfaces* **16**, 49262–49274 (2024).
50. Denisov, N., Yoo, J. E. & Schmuki, P. Effect of different hole scavengers on the photoelectrochemical properties and photocatalytic hydrogen evolution performance of pristine and Pt-decorated TiO_2 nanotubes. *Electrochim. Acta* **319**, 61–71 (2019).
51. Zhang, L., Zhang, J., Yu, H. & Yu, J. Emerging S-scheme photocatalyst. *Adv. Mater*. **34**, 2107668 (2022).
52. Mao, Y. et al. Interfacial polarons in van der Waals Heterojunction of Monolayer $SnSe_2$ on $SrTiO_3$ (001). *Nano Lett.* **20**, 8067–8073 (2020).
53. Vurgaftman, I., Meyer, J. R. & Ram-Mohan, L. R. Band parameters for III-V compound semiconductors and their alloys. *J. Appl. Phys.* **89**, 5815–5875 (2001).
54. Bockris, J. O. & Otagawa, T. The electrocatalysis of oxygen evolution on perovskites. *J. Electrochem. Soc.* **131**, 290–302 (1984).
55. Favaro, M. et al. Elucidating the alkaline oxygen evolution reaction mechanism on platinum. *J. Mater. Chem. A Mater.* **5**, 11634–11643 (2017).
56. Nørskov, J. K. et al. Origin of the overpotential for oxygen reduction at a fuel-cell cathode. *J. Phys. Chem. B.* **108**, 17886–17892 (2004).
57. Talha Aqueel Ahmed, A. et al. Hybridized heterostructure of CoS and MoS_2 nanoparticles for highly-efficient and robust bifunctional water electrolysis. *Appl. Surf. Sci*. **592**, 153196 (2022).
58. Huang, X., Wang, J., Tao, H. B., Tian, H. & Xu, H. An essential descriptor for the oxygen evolution reaction on reducible metal oxide surfaces. *Chem. Sci.* **10**, 3340–3345 (2019).
59. Exner, K. S. Four generations of volcano plots for the oxygen evolution reaction: beyond proton-coupled electron transfer steps? *Acc. Chem. Res.* **57**, 1336–1345 (2024).
60. Kresse, G. & Hafner, J. Ab initio molecular dynamics for liquid metals. *Phys. Rev. B* **47**, (1993).
61. Kresse, G. & Hafner, J. Ab initio molecular-dynamics simulation of the liquid-metal-amorphous-semiconductor transition in germanium. *Phys. Rev. B* **8**, 14251–14296 (1994).
62. Kresse, G. & Furthmüller, J. Efficient iterative schemes for ab initio total-energy calculations using a plane-wave basis set. *Phys. Rev. B* **54**, 11169–11185 (1996).
63. Joubert, D. From ultrasoft pseudopotentials to the projector augmented-wave method. *Phys. Rev. B Condens. Matter Mater. Phys.* **59**, 1758–1775 (1999).
64. Blöchl, P. E. Projector augmented-wave method. *Phys. Rev. B* **50**, 17953–17979 (1994).
65. Perdew, J. P. et al. Restoring the density-gradient expansion for exchange in solids and surfaces. *Phys. Rev. Lett.* **100**, 1–4 (2008).
66. Methfessel, M. & Paxton, A. T. High-precision sampling for Brillouin-zone integration in metals. *Phys. Rev. B* **40**, 3616–3621 (1989).
67. Pack, J. D. & Monkhorst, H. J. Special points for Brillouin-zone integrations. *Phys. Rev. B* **16**, 1748–1749 (1977).
68. Kronberg, R. & Laasonen, K. Reconciling the experimental and computational hydrogen evolution activities of Pt(111) through DFT-based constrained MD simulations. *ACS Catal.* **11**, 8062–8078 (2021).
69. Liu, X. et al. Understanding trends in electrochemical carbon dioxide reduction rates. *Nat. Commun.* **8**, 1–7 (2017).
70. Man, I. C. et al. Universality in oxygen evolution electrocatalysis on oxide surfaces. *ChemCatChem* **3**, 1159–1165 (2011).
71. Li, J. Oxygen evolution reaction in energy conversion and storage: design strategies under and beyond the energy scaling relationship. *Nano-Micro Lett*., **14** (2022).
72. Huang, Z. F. et al. Strategies to break the scaling relation toward enhanced oxygen electrocatalysis. *Matter* **1**, 1494–1518 (2019).
73. Viswanathan, V., Hansen, H. A., Rossmeisl, J. & Nørskov, J. K. Universality in oxygen reduction electrocatalysis on metal surfaces. *ACS Catal.* **2**, 1654–1660 (2012).
74. Christensen, R., Hansen, H. A., Dickens, C. F., Nørskov, J. K. & Vegge, T. Functional independent scaling relation for ORR/OER catalysts. *J. Phys. Chem. C.* **120**, 24910–24916 (2016).
75. Altieri, R. et al. Development of an automated SILAR method for the sustainable fabrication of BiOI/TiO_2 photoanodes. *Energy Adv.* **3**, 2564 (2024).
76. Vensaus, P. et al. CoPi-modified mesoporous titania photoelectrodes for water splitting: why less is more. *ACS Appl. Eng. Mater.* **2**, 224–235 (2024).
77. Liu, C. et al. Efficient photoelectrochemical water splitting by g-C_3N_4/TiO_2 nanotube array heterostructures. *Nanomicro Lett.* **10**, 1–13 (2018).

Author contributions

V.R.: Writing—original draft, review and editing, investigation, material's synthesis, photoelectrochemical characterization. V.P.: Writing—original draft, review and editing, microstructural characterization, visualization; L.S.: investigation, material's synthesis, microstructural characterization, formal analysis. L.L.: investigation, material's characterization. C.M.: Investigation, Software, DFT Simulation. R.D.: Investigation, Software, DFT Simulation. C.M.C: Investigation, Validation, Software, DFT Simulation. P.I.: Validation, Writing—review and editing. L.M.: Supervision, Writing—review and editing, Funding acquisition. C.C.: Finalizing, Writing—original draft, Funding Acquisition, Supervision.

Funding
C.C. acknowledges the financial support from PRIN 2022 project #2022LZWKAJ CUP E53D23005280006 and from PRIN 2022 -PNRR project #P2022JRB2Y CUP E53D23017740001.

Competing interests
The authors declare no competing interests.

Additional information
Supplementary information The online version contains supplementary material available at https://doi.org/10.1038/s41699-026-00721-1.

Correspondence and requests for materials should be addressed to Vittorio Ricci or Valentina Paolucci.

Reprints and permissions information is available at http://www.nature.com/reprints

Publisher's note Springer Nature remains neutral with regard to jurisdictional claims in published maps and institutional affiliations.

Open Access This article is licensed under a Creative Commons Attribution 4.0 International License, which permits use, sharing, adaptation, distribution and reproduction in any medium or format, as long as you give appropriate credit to the original author(s) and the source, provide a link to the Creative Commons licence, and indicate if changes were made. The images or other third party material in this article are included in the article's Creative Commons licence, unless indicated otherwise in a credit line to the material. If material is not included in the article's Creative Commons licence and your intended use is not permitted by statutory regulation or exceeds the permitted use, you will need to obtain permission directly from the copyright holder. To view a copy of this licence, visit http://creativecommons.org/licenses/by/4.0/.

© The Author(s) 2026